An Extended Numerical Manifold Method for Unsaturated Soil-water Interaction Analysis at Micro-scale

Hao Sun[a,b], Zhijun Wu[a,*], Liange Zheng[b], Yongtao Yang[c], Da Huang[d], Longxiao Guo[e]

a. School of Civil Engineering, Wuhan University, Wuhan 430072, China

b. Energy Geosciences Division, Earth & Environmental Sciences Area, Lawrence Berkeley National Laboratory, Berkeley, CA 94720, USA

c. State Key Laboratory of Geomechanics and Geotechnical Engineering, Institute of Rock and Soil Mechanics, Chinese Academy of Sciences, Wuhan 430071, China

d. School of Civil and Transportation Engineering, Hebei University of Technology, Tianjin 300401, China

e. Department of Civil and Structural Engineering, Kyushu University, Fukuoka 819-0395, Japan

Abstract

To investigate unsaturated soil-water interaction at micro-scale, this study extends the numerical manifold method (NMM) by incorporating a soil-water coupling model considering specific capillary water distribution and capillary force calculation. The soil skeleton is constructed by a soil skeleton generation algorithm with random polygons. To more realistically capture the interaction between soil grains and capillary water, a capillary mechanics-based geometric algorithm is proposed to iteratively calculate the capillary water distribution of the unsaturated soil system. The capillary forces corresponding to the capillary water distribution are calculated based on the Young-Laplace equation. The proposed capillary water solving framework is first verified by reproducing the soil-water characteristic curve and the capillary water distribution of an ideal contact-disk model against analytical solutions. Then an ideal direct shear test is performed to further validate the two-way soil-water coupling procedure, in which a comparison of the numerical and analytical relationship between shear strength and matric suction is presented. Finally, based on the extended method a series of microscopic simulations are conducted on two soil specimens with same

* Corresponding author at: School of Civil Engineering, Wuhan University, Wuhan 430072, China

Email address: zhijunwu@whu.edu.cn (Zhijun Wu)

porosity and mean grain diameter but different uniformity coefficients to investigate their hydraulic and mechanical characteristics at micro-scale. The hydraulic test results show that their soil-water characteristic curves are generally close. In addition, for both specimens, there is a close correlation among its matric suction, the number of capillary meniscuses and effective stress parameter, which is further explained from a microscopic perspective. The compression test results show that due to the capillary forces between soil grains, capillary water can enhance the stiffness of unsaturated soil against compression. Furthermore, the compaction of soil skeleton structure has significant effects on the hydraulic characteristics of unsaturated soil.

Keywords: Numerical manifold method; Unsaturated soil; Capillary water; Soil-water interaction; Microscopic analysis

1. Introduction

Unsaturated soils, in which pores between the soil skeleton are occupied by both liquid and gas phases, are widely distributed on the earth's surface and involved in most engineering practice, especially in arid/semi-arid areas [1]. Many natural and engineering disasters such as landslides and debris flow are often caused by the strength reduction of unsaturated soils following the change of water content [2]. It is therefore important to understand the mechanical behaviour of unsaturated soils. Unsaturated soil, unlike saturated soil, involves complex interactions among the three constituent phases at the micro-scale level, and its mechanical behaviour is subsequently controlled not merely by soil grains arrangement, density, and history of the soil skeleton like saturated soils, but also by the soil suction. The capillary force acted at the water-air interface is one of the essential components of soil suction and its distribution is dependent on the capillary water distribution that is strongly influenced by soil microstructure. Thus, to better interpret the macroscopic behaviour of unsaturated soils, its microscopic mechanism should be studied by taking the capillary water distribution, as well as its interactions with the soil skeleton into consideration.

Unsaturated soil mechanics was historically developed based on saturated soil

mechanics. Briggs [3] used the surface tension to explain the water-holding capacity of soil at early times. Further, Haines [4] considered surface tension as a positive factor for increasing the stress among soil grains, which was interpreted by a capillary model. Based on the effective stress principle proposed by Terzaghi [5], Bishop [6] put forward an effective stress equation for the description of unsaturated soils by introducing the capillary action. Later, to account for the shear strength of unsaturated soil, a series of shear strength equations for unsaturated soil were derived based on experimental data, which can be classified as a single-variable theory [7], or a double-variable theory [8]. However, calibrating the parameters required by the above shear strength equations for practical engineering was challenging due to the difficulty of measuring matric suction and material parameters vaguely related to matric suction. In addition, the strength behaviour of unsaturated soils can be only captured over a small range of suction scale when being compared with the experimental observations [8-11].

With the extensive application of micromechanics in the theoretical analysis of unsaturated soils, several microscopic analyses based on the ideal soil model (spherical or circular grain assembly) were carried out for unsaturated soils. Intergranular force contains a contribution from surface tension in addition to matric suction was first Fisher [12]. Based on Fisher's study, a general stress equation available for colloidal soils, non-pendular water, and occluded bubbles was derived by Sparks [13], in which the influence of changing wetting angles was considered. Cho and Santamarina [14] focused on the pendular stage and the effect of capillary forces on small strain stiffness of unsaturated soils and illustrated several phenomena related to the evolution of capillary forces during drying. Lian et al. [15] and Mason et al. [16] studied the mechanical behavior of the liquid bridge shared by spheres. The hysteresis of capillary stress in unsaturated soil was studied by Likos and Lu [17] to interpret the soil behaviour in wetting and drying processes. Wan et al. [18] proposed an effective stress equation in the tensor form to determine the relationship between the degree of saturation and effective stress parameter. The free energy approach and toroidal approximation were employed by Lechman and Lu [19] to calculate the normalized capillary force and water retention. In addition to the ideal soil model used above, Li

[20] adopted an assembly of rigid grains of arbitrary shape to investigate effective stress and further proposed the quasi-effective stress for unsaturated soils corresponding to the effective stress for saturated soils. The microscopic analyses shed light on the microscopic mechanisms that have deepened the understanding of the macroscopic behaviour of unsaturated soil and formed the theoretical basis for modelling unsaturated soil at micro-scale.

In parallel with theoretical development, experimental studies are certainly another pillar to study the mechanical processes of unsaturated soils, and a large number of experimental investigations have been conducted [1]. However, the conventional laboratory investigations can hardly capture the microscopic behaviors of unsaturated soils even with some advanced experimental techniques such as the photoelasticity technique [21] and X-ray computerized tomography [22]. As an alternative tool, numerical methods [23], which can conveniently deal with complex model geometry and boundary conditions [24, 25], are widely adopted for numerically investigating the mechanical behaviour of unsaturated soils. Due to the discontinuity of soil skeleton and complexity of capillary action, continuum-based numerical methods represented by the finite element method (FEM) [26, 27], which are often applied to macroscopic analysis on unsaturated soils [28-31], can hardly realistically represent unsaturated soils at micro-scale. As a discontinuum-based method, the discrete element method (DEM) [32], which mostly represents soils by bonded circular (2D) or spherical (3D) grains with random packing, is one of the most representative methods for examining the mechanical behaviour of soils at present [33-39]. With the modified contact models considering the capillary forces, the DEM was further used for microscopic analysis on unsaturated soils to reveal the microscopic mechanism of the strength and deformation behavior under capillary action [1, 2, 40-45]. However, circular or spherical grains cannot realistically represent soil skeleton and will significantly weaken the interlocking effect of real soil grains. Besides, the capillary water assumptions required in the DEM simulations such as toroidal approximation and no capillary force between non-contacting grains reduce the accuracy of predicting capillary water distribution and capillary forces calculation. Unlike the above DEM, the soil skeleton can be built with

polygonal grains of arbitrary shape by discontinuous deformation analysis (DDA) [46-48] which can better capture the interactions between soil grains. Further, the DDA was extended to analyze unsaturated soil-water interaction by introducing a capillary water algorithm [49]. Radjai and Richefeu [50] used the contact dynamics (CD) method, which deals with the motion of multi-body systems subjected to unilateral contacts and friction, to verify their proposed relationship between Coulomb cohesion of unsaturated soil and its intergranular capillary bonds distribution.

The numerical manifold method (NMM) [51, 52], which integrates the continuum-based method FEM and discontinuum-based method DDA in a unified framework, has powerful capabilities in modelling rock failure process involving continuous-discontinuous behaviour [53-61]. However, most NMM-based studies focused on the macroscopic behaviour of rocks regardless of its microscopic mechanisms. To analyze the rock behavior at micro-scale, Wu et al. [62] proposed a micro-mechanical based NMM by considering rock microstructure as well as the interaction and cracking of rock micro-grains. By incorporating a coupled hydro-mechanical model, the micro-mechanical based NMM was extended for hydraulic fracturing modelling at micro-scale [63]. From its unique hybrid characteristics and excellent performance in rock microscopic analysis [54, 62, 63], the NMM shows the following considerable potentials in soil microscopic modelling: (1) With the adoption of the simplex integration method, soil grains of arbitrary shape can be considered for more realistically representing soil skeleton; (2) By the NMM contact technique, the interaction and motion of soil grains can be accurately captured; (3) As a block composed of multiple manifold elements, the deformation of soil grain can be obtained with higher accuracy compared with the DDA using constant strain blocks (4) based on the two covers system, an explicit representation of transgranular cracking of soil grains can be straightforwardly achieved. However, at present, the NMM has no application in soil microscopic analysis. And no capillary water algorithm was proposed for the NMM, which restricts its capacity to simulate unsaturated soils at micro-scale.

Therefore, in this study, to investigate the unsaturated soil-water interaction at micro-scale, a soil-water coupling scheme is proposed based on the NMM framework.

A soil skeleton generation algorithm is first employed to construct soil skeleton with soil grains of arbitrary shape. Then, a capillary mechanics-based geometric algorithm is developed to iteratively calculate the capillary water distribution of the unsaturated soil system, and its corresponding capillary forces are calculated based on the Young-Laplace equation. For modelling the soil-water interaction, a two-way coupling procedure is achieved by performing the mechanical solver (NMM) and the capillary solver alternately in each time step. The extended method is then verified by two ideal models against analytical solutions. Finally, a series of microscopic simulations are conducted on two soil specimens with the same porosity and mean grain diameter but different uniformity coefficients to investigate their hydraulic and mechanical characteristics at micro-scale. The results elucidate that the extended method can simulate robustly the hydraulic and mechanical behaviours of unsaturated soil at micro-scale and capture the evolution of microscopic parameters such as the number of capillary meniscuses and effective stress parameter.

2. NMM for Soil Skeleton Modelling

This section presents the main characteristics of the NMM for modelling the unsaturated soil-water interaction at micro-scale. As a pre-processor, the soil skeleton generation algorithm is adopted to build soil skeleton with random polygons. In the NMM, the random polygons are treated as independent loops (grains) consisting of several manifold elements, which define the shapes and boundaries of soil grains as well as the contacts between them. Based on the finite cover system, continuous-discontinuous behaviours of the soil grains such as deformation and motion can be modelled in a unified framework. Besides, the interaction between adjacent soil grains is captured by the grain-based contact algorithm.

2.1 Finite Cover System

As partition of unity (PU)-based numerical method, the numerical manifold method (NMM) proposed by Shi [52] can be identified as a unified framework integrating the finite element method (FEM) and discontinuous deformation analysis

(DDA) [64]. The core and most innovative characteristic of the NMM is the finite cover (mesh) system composed of the mathematical cover (MC) and physical cover (PC), based on which the continuous-discontinuous problems can be solved with high efficiency. The mathematical cover, which is a set of user-defined overlapping unions of mathematical patches of arbitrary shape, must cover the entire problem domain without omission. In the NMM, the physical mesh is a unique portrait of the problem domain, including physical components such as the external boundaries, holes, block boundaries, material interfaces, and internal discontinuities, etc. By intersecting the mathematical patches with the physical components of the problem domain, all of the physical patches are obtained and form the physical cover together. It should be noted that each mathematical patch is divided into at least one physical patch and the overlapping or independent regions of them define the manifold elements (MEs) of the NMM.

The illustration for generation procedures of the finite cover system and MEs described above are given in Fig. 1. The whole problem domain (purple area) is completely covered by the mathematical cover consisting of a set of overlapped regular hexagonal mathematical patches. For example, M_a, M_b and M_c are three mutually independent mathematical patches and have a triangle region in common. The physical components of the problem domain contain an external boundary Γ_u and an internal discontinuity Γ_D. Then, by intersecting the mathematical patches with the physical components, for example, the mathematical patch M_a intersecting with both the external boundary Γ_u and the internal discontinuity Γ_D forms the physical patches $P_{a\text{-}1}$ and $P_{a\text{-}2}$. Similarly, the physical patches $P_{b\text{-}1}$ and $P_{b\text{-}2}$ are generated from mathematical patch M_b intersecting with the internal discontinuity Γ_D and the physical patches $P_{c\text{-}1}$ and $P_{c\text{-}2}$ are generated from mathematical patch M_c intersecting with both the external boundary Γ_u and the internal discontinuity Γ_D. Finally, the MEs are obtained with overlapping of these formed physical patches; for example, MEs E_m and E_n are generated from the common region of physical patches $P_{a\text{-}1}$, $P_{b\text{-}1}$ and $P_{c\text{-}1}$ and that of physical patches $P_{a\text{-}2}$, $P_{b\text{-}2}$ and $P_{c\text{-}2}$, respectively as shown in Fig. 1.

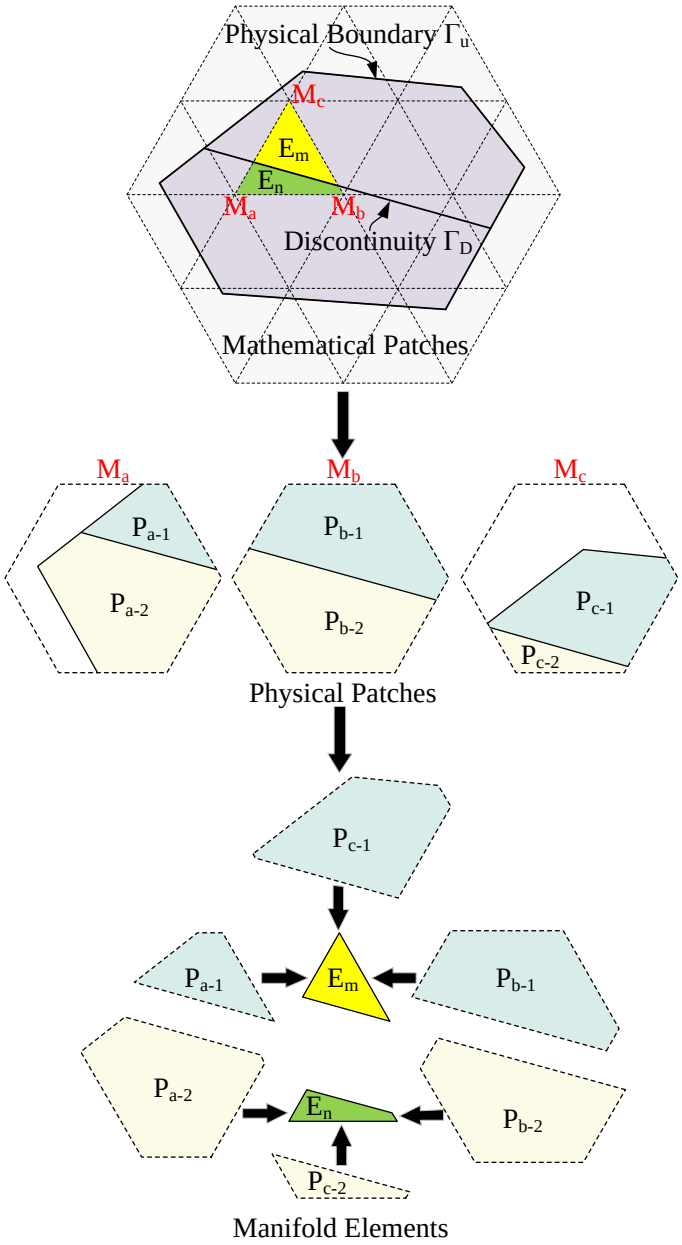

Fig. 1. Illustration of the finite cover system

Based on the generated finite cover system, the local approximation functions $u_i^h(r)$ is defined independently for individual physical patch P_i. Then, by connecting the local approximation functions together with a weight function, the global displacement function on individual ME can be expressed as:

$$U^h(r) = \sum_{i=1}^{n} w_i(r) u_i^h(r) \tag{1}$$

where n denotes the number of physical patches, r is the position vector, and $w_i(r)$ is the weight function on P_i. In addition to the continuous problems, the discontinuous

behaviours can also be directly solved with the finite cover system described above. For example, according to Eq. (1), the displacement functions of elements E_m and E_n can be expressed respectively as:

$$\begin{cases} U_{E_{\mathrm{m}}}^{h}(r) = w_{\mathrm{P_{a\text{-}1}}}(r)u_{\mathrm{P_{a\text{-}1}}}^{h}(r) + w_{\mathrm{P_{b\text{-}1}}}(r)u_{\mathrm{P_{b\text{-}1}}}^{h}(r) + w_{\mathrm{P_{c\text{-}1}}}(r)u_{\mathrm{P_{c\text{-}1}}}^{h}(r) \\ U_{E_{\mathrm{n}}}^{h}(r) = w_{\mathrm{P_{a\text{-}2}}}(r)u_{\mathrm{P_{a\text{-}2}}}^{h}(r) + w_{\mathrm{P_{b\text{-}2}}}(r)u_{\mathrm{P_{b\text{-}2}}}^{h}(r) + w_{\mathrm{P_{c\text{-}2}}}(r)u_{\mathrm{P_{c\text{-}2}}}^{h}(r) \end{cases} \tag{2}$$

Then, the displacement discontinuity across the interface Γ_D between elements E_3 and E_4 can be captured as:

$$U_{\Gamma_{\mathrm{D}}}(r) = U_{E_{\mathrm{m}}}^{h}(r) - U_{E_{\mathrm{n}}}^{h}(r) \tag{3}$$

For a linear elastic problem with discontinuities, the weak form of NMM governing equation can be derived from the Galerkin formulation [65] as follows:

$$\begin{aligned} &\int_{\Omega^h} \sigma\left(u^h\right)\cdot\varepsilon\left(\delta u^h\right)d\Omega + \int_{\Omega^h}\rho\ddot{u}^h\cdot\delta u^h d\Omega + \lambda\int_{\Gamma_u^h}\left(u^h-\bar{u}\right)\cdot\delta u^h d\Gamma \\ &= \int_{\Gamma_{\mathrm{b}}^h}\delta u^h\cdot p d\Gamma + \int_{\Gamma_{\mathrm{t}}^h}\bar{t}\cdot\delta u^h d\Gamma + \int_{\Omega^h} b\cdot\delta u^h d\Omega \end{aligned} \tag{4}$$

where σ and ε are the stress and strain tensors, respectively; Ω^h is the problem domain subjected to the body force b; λ is the real penalty value; $\bar{u}$ and $\bar{t}$ are the displacement and traction conditions on the corresponding boundaries Γ_u^h and Γ_{t}^h, respectively; ρ is the material density; and p is the intergranular contact force on the grain boundary Γ_{b}^h, which can be captured by a grain-based contact model introduced in Section 2.3.

2.2 Construction of Soil Skeleton Model

To microscopically construct the soil skeleton in the NMM, a soil skeleton generation algorithm [66] is employed as a pre-processor, which can be divided into two parts: soil grain generating and packing. First, the soil grains are generated as random polygons by controlling their number and size according to the preset grain size distribution. And then the generated soil grains are successively packed into the specimen area by a soil grain packing algorithm. For the generated soil skeleton, the computational model in the NMM can be obtained through the procedures illustrated in Fig. 2. As a kind of physical component, all grains boundaries of the soil skeleton in

Fig. 2(a) are intersected with the corresponding mathematical cover in Fig. 2(b) to generate independent loops (grains) consisting of several manifold elements and eventually the corresponding grain-based computational model in Fig. 2(c). Based on the generated grain-based computational model, the mechanical behaviour of the soil skeleton involving both motion and deformation of the soil grains can be simulated more realistically at micro-scale.

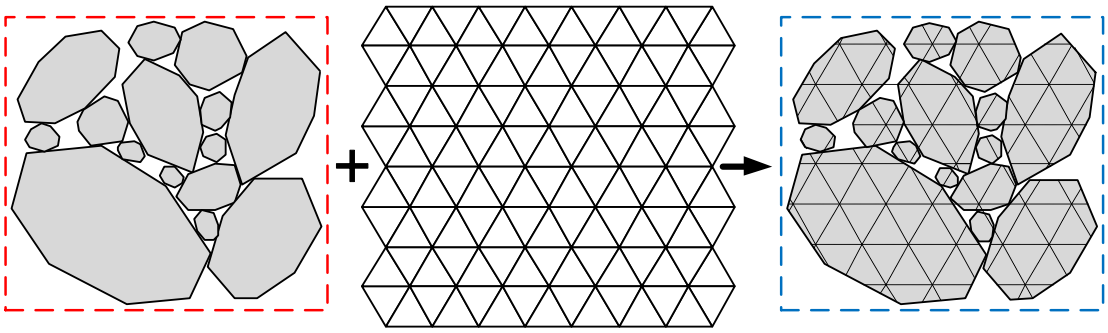

Fig. 2. Construction procedure of soil skeleton computational model (a) random polygonal grains assembly (b) corresponding mathematical cover (c) grain-based computational model

2.3 Grain-based Contact Model

For capturing the intergranular interactions with high efficiency, a grain-based contact model is adopted instead of the original NMM contact model [63]. As basic contact units, the grains as shown in Fig. 2(c) are simplified as closed domains encompassed by corner vertices on the boundaries and then detected by a contact detection algorithm at each time step to search possible intergranular contacts. As shown in Fig. 3, there are three types of intergranular contacts including angle to angle, angle to edge and edge to edge. Furthermore, an edge-edge contact such as edge V_1V_2 to edge V_3V_4 can be further decomposed into two angle-edge contacts with angle V_1 to edge V_3V_4 and angle V_4 to edge V_1V_2, as shown in Fig. 3(c). Then, with the contact type identified, the contact status of a intergranular contact can be judged, by both the relative normal displacement w between grains and Coulomb friction law. According to the contact status, the intergranular interactions, i.e. interactive normal and tangential

forces F_n and F_s can be calculated by a force-displacement model as follows:

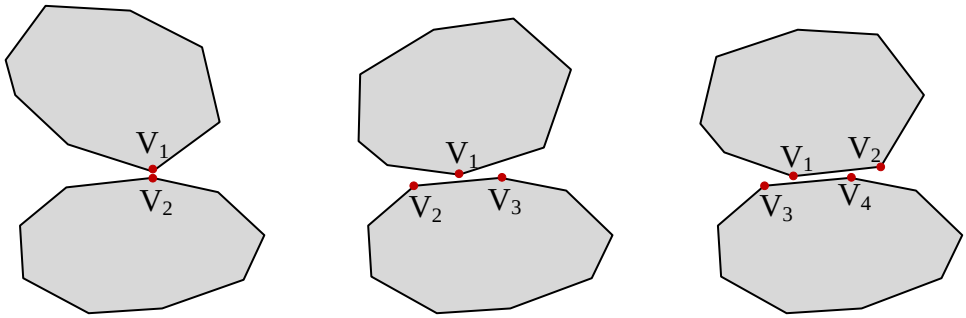

Fig. 3. Three types of intergranular contacts (a) angle to angle (b) angle to edge (c) edge to edge

For the ‘‘open’’ contact status ($w > 0$),

$$F_n = F_s = 0 \tag{5}$$

and for the “locked” contact status ($w \le 0$, $F_s \le F_n \cdot \tan\varphi$),

$$\begin{cases} F_n = k_n w \\ F_s = k_s s \end{cases} \tag{6}$$

and for the ‘‘sliding’’ contact status ($w \le 0$, $F_s > F_n \cdot \tan\varphi$),

$$\begin{cases} F_n = k_n w \\ F_s = F_n \cdot \tan\varphi \end{cases} \tag{7}$$

where k_n and k_s are the normal and tangential contact stiffness, respectively; s is the relative tangential displacement of the intergranular contact; φ is the friction angle of the contact interface.

3. Extension Scheme of NMM for Unsaturated Soil-water Coupling

In this section, the basic theory of capillary mechanics and assumptions used in this study are first introduced. Based on the capillary mechanics, a geometric algorithm is proposed by iteratively calculating the capillary water distribution of the unsaturated soil system. Then the intergranular capillary forces can be determined by the Young-Laplace equation. With stress boundary conditions due to the capillary forces obtained

from the capillary solver, both the motion and deformation of soil grains system can be captured by the mechanical solver (NMM), based on which the capillary water distribution and its corresponding capillary forces are further updated. Finally, by performing the mechanical solver (NMM) and the capillary solver alternately with the time step, a two-way coupling method can be obtained to model unsaturated soil-water interaction. The basic theory of capillary mechanics, the detailed process of implementing the capillary water solving framework as well as the coupling procedure are sequentially described below.

3.1 Theory and Assumptions for Capillary Water in Unsaturated Soil

Based on Terzaghi's effective stress equation for saturated soils, Bishop [6] proposed the effective stress equation for unsaturated soils as follows:

$$\sigma' = \sigma - u_a + \chi(u_a - u_w) \tag{8}$$

where σ' is effective normal stress; σ is total normal stress; u_a is pore-air pressure; u_w is pore-water pressure; χ is an effective stress parameter. The difference ($u_a - u_w$) in the equation above is matric suction S_m, which can be calculated by Young-Laplace equation [12, 49] as:

$$S_m = u_a - u_w = T_s(\frac{1}{r_1} + \frac{1}{r_2}) \tag{9}$$

where T_s is the surface tension; r_1 and r_2 are two principal curvature radii of the water-air interface which separates the capillary water from pore-air and is also called meniscus. In two-dimensions, the capillary meniscus (water-air interface) only has one principal curvature radius r due to the other one with infinite value, such that Young-Laplace equation can be simplified as:

$$S_m = u_a - u_w = T_s \frac{1}{r} \tag{10}$$

It can be concluded from Eq. (10) that the larger the curvature radius of capillary meniscus r, the smaller the matric suction S_m. As shown in Fig. 4, the capillary water as a liquid bridge is located between two parallel solid plates and has two meniscuses of the same curvature radius. θ_1 and θ_2 are contact angles between capillary water and

the upper and lower plate respectively, the values of which depend on the material property of solid plates. Moreover, the surface tension is mainly determined by both liquid type and its temperature, for example, the surface tension of water is 72.75 mN/m at a temperature of 20 ℃.

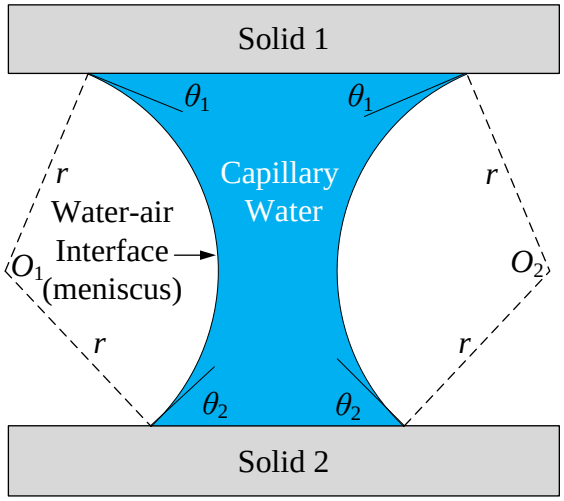

Fig. 4. Illustration of liquid bridge system

The soil grains are combinations of several minerals, which leads to multiple cleavage surfaces distributed along the grain boundary. Moreover, accompanied by the contact angle hysteresis, there is capillary water migration through the water network of unsaturated soil. The above complex characteristics bring great difficulties to the numerical calculation. For simplification, three assumptions were proposed in this study as (1) the contact angle hysteresis is not considered on the surfaces of soil grains; (2) regardless of the difference of the cleavage surface on the soil grain boundary, the contact angle is the same at any position of the boundary. (3) at each time step, the capillary water distributed throughout the unsaturated soil system is in steady-state without the seepage of capillary water (such that all capillary water has the same pressure in the unsaturated soil system; all pore-air has the same pressure in the unsaturated soil system; and there is also an equilibrium between the evaporation of water and condensation of vapor at any capillary meniscus). From the above assumptions, it can be concluded that the curvature radii of the capillary meniscuses are

the same in the whole unsaturated soil system.

3.2 Capillary Water Solving Framework

Different from saturated soil analysis, the capillary water distribution, which determines both the magnitude and position of soil-water interaction, is significantly important and must be considered in microscopic analysis for unsaturated soil. Therefore, under the assumptions mentioned above, a capillary mechanics-based geometric algorithm is first proposed to obtain the capillary water distribution of the unsaturated soil system. In each time step, the geometric algorithm illustrated in Fig. 5 is performed to update the capillary water distribution. Before executing the algorithm, the contact angles of grains and water content V_w of soil system should be given, and the curvature radius r of capillary meniscus needs to be assigned an initial value. Then, according to the parameters set above, the center trajectory of capillary meniscus (*abbr. CT*) is drawn for each grain. The potential capillary meniscuses can be positioned by taking the intersections of *CT*s as the centers of potential capillary meniscuses. Furthermore, capillary meniscuses with convex shape will be eliminated as invalid meniscuses. With the capillary water distribution generated above, the total volume of capillary water V_r is calculated and then compared with the pre-set V_w. If $V_r = V_w$, both qualified capillary water distribution and r are achieved and the algorithm will be terminated. Otherwise, the value of r will be adjusted and the above process will be continually repeated until $V_r = V_w$.

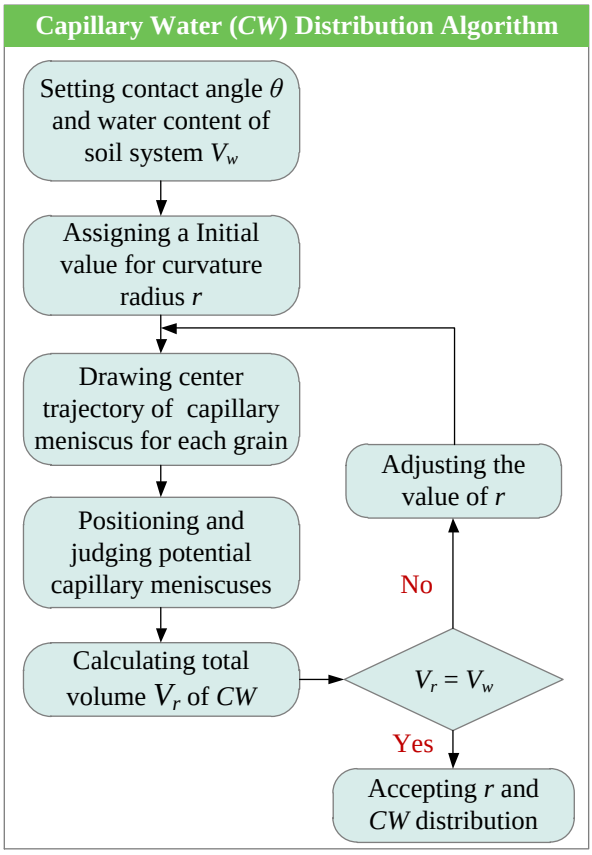

Fig. 5. Iterative algorithm for calculating capillary water distribution

To interpret the process of searching the capillary meniscus in detail, a two-grains system is employed as an example, as shown in Fig. 6. The contact angles of Grains 1 and 2 are θ_1 and θ_2, respectively. The liquid bridge shared by Grains 1 and 2 has two capillary meniscuses of curvature radius r, m_1 and m_2. The positions of m_1 and m_2 are controlled by their centers O_1 and O_2, respectively. Therefore, to search the capillary meniscus, all possible centers of capillary meniscus i.e. *CT* need to be found out. It can be seen from Fig. 6 that for the right meniscus, the directions of P_{s1}-O_1 and outer normal of the edge of P_{s1} differ by θ_1 anticlockwise, and the directions of P_{e1}-O_1 and outer normal of the edge of P_{e1} differ by θ_2 clockwise. And, for the left meniscus, the directions of P_{s2}-O_2 and outer normal of the edge of P_{s2} differ by θ_1 clockwise, and the directions of P_{e2}-O_2 and outer normal of the edge of P_{e2} differ by θ_2 anticlockwise. In addition, the distance between each endpoints and its corresponding center of capillary meniscus is r. According to the above geometrical relationships between endpoint and center of capillary meniscus, the *CT* for each grain can be determined by locating the

possible center of capillary meniscus corresponding to each point on grain boundary, as shown in Fig. 7. It should be noted that the corner vertices of grain boundary are considered as rounded corners with a tiny radius, such that the parts of *CT* at the corners are arcs with radius *r*. Since for the two-grains system, there are two types of geometrical relationships from right and left meniscuses respectively, two different pairs of *CT*s can be achieved as shown in Figs. 7(a) and (b). By taking the intersections of *CT*s as the centers of capillary meniscuses, the potential capillary meniscuses can be further positioned. As shown in Fig. 7, four capillary meniscuses are positioned, but the two with convex shape will be eliminated as invalid meniscuses. And the remaining two are the capillary meniscuses m_1 and m_2 as shown in Fig. 6.

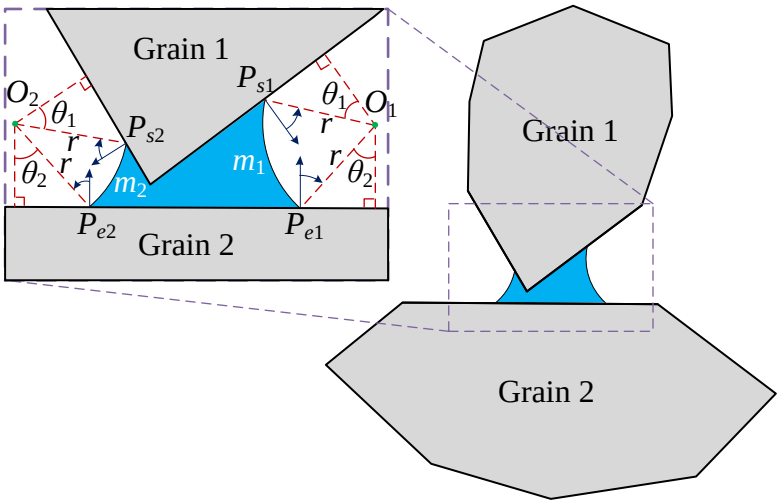

Fig. 6. Geometrical relationship between endpoints and center of capillary meniscus

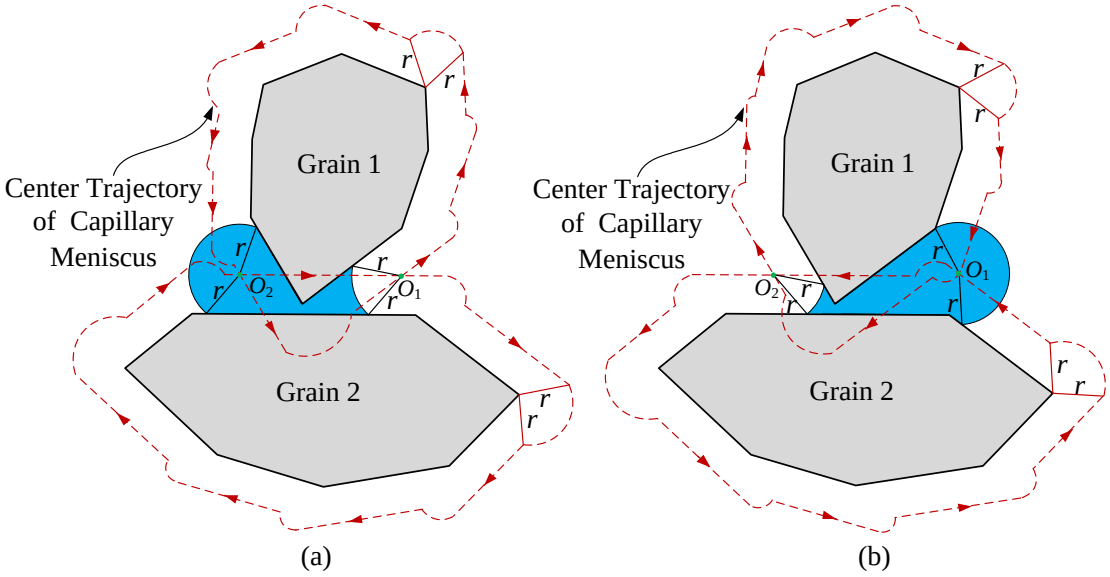

Fig. 7. Searching the potential capillary meniscus by *CT*

A multi-grains system with n (n > 2) grains can be decomposed into C_n^2 ($C_n^2 = n!/2!(n-2)!$) two-grains systems described above, and thus its capillary water distribution is formed by liquid bridges of the C_n^2 two-grains systems. For example, as shown in Fig. 8(a), the capillary water distribution of a three-grains systems has three liquid bridges from grain pairs 1-2, 1-3 and 2-3, respectively. $m_{a\text{-}f}$ represent meniscuses of the three liquid bridges. However, with the increase of water content as shown in Fig. 8(b), the meniscuses m_b, m_d and m_e will meet each other to generate three overlapping areas and an enclosed bubble which has no contribution to the soil suction. Therefore, the overlapping areas due to the fusion of meniscuses will be deleted. In addition, the fused meniscuses m_b, m_d and m_e and surface tension induced by them will not be considered.

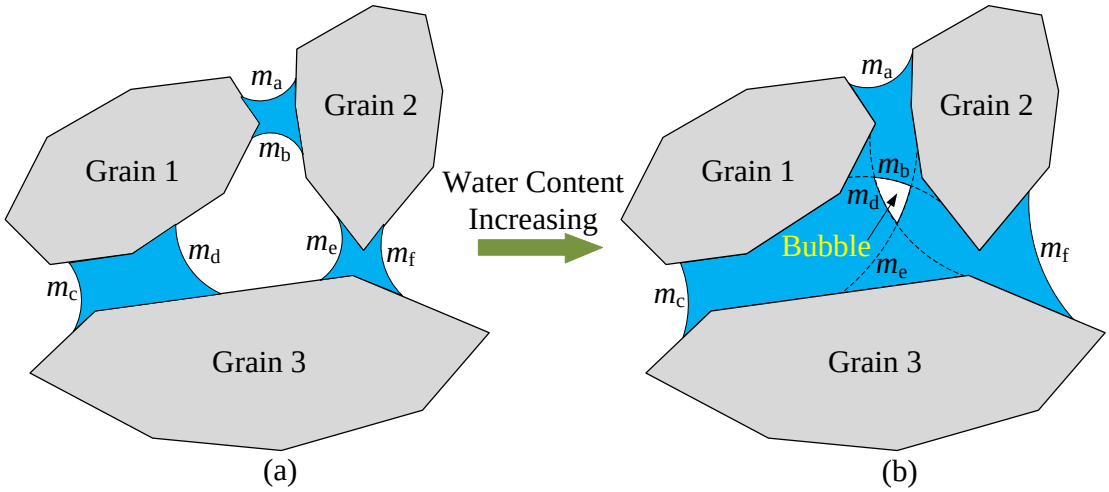

Fig. 8. Capillary water distribution of multi-grains system

According to the capillary water distribution generated by the geometric algorithm above, the capillary forces are applied to the grain boundaries occupied by the capillary water. The capillary force includes contributions from both the matric suction S_m and the surface tension T_s of the capillary meniscus. As shown in Fig. 9, a liquid bridge is shared by Grains A and B. The matric suction (blue arrows) as a uniformly distributed load is exerted on the normal direction of each boundary segment where the capillary water is distributed. As a concentrated force, the surface tension (red arrows) tangent to the capillary meniscus acts on the intersection point of three-phase (soil skeleton, pore-water and pore-air) boundaries. Finally, the above two types of forces acting on the grains are transformed into nodal forces of the manifold elements. The specific method of force transformation can be found in the reference [67].

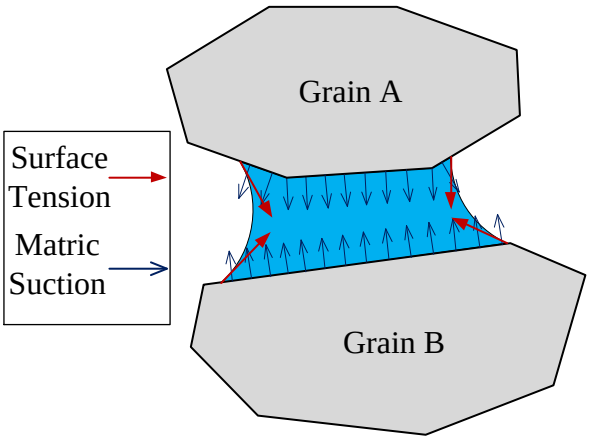

Fig. 9. Capillary forces exerted on the soil grains

3.3 Soil-water Coupling Procedure

To extend the NMM for modelling unsaturated soil-water interaction, a two-way coupling procedure for capillary water and soil grains is implemented, which alternately executes the mechanical solver (NMM) and the capillary solver in each time step. As shown in Fig. 10, the soil skeleton model is first generated by the soil skeleton generation algorithm mentioned above. Then, the calculation parameters corresponding to the two solvers are set. With the soil skeleton model and calculation parameters, the capillary water distribution is initialized for the first time step and will be successively updated by the capillary water distribution algorithm at each later time step based on the new geometry of soil skeleton given by the mechanical analysis of the last time step. Based on the determined distribution of capillary water, the capillary forces consisting of both the surface tension and matric suction are then calculated and applied on each boundary segment occupied by the capillary water at each time step. Then, the calculated surface tension and matric suction are respectively taken as an external uniformly distributed and concentrated loads acting on the boundaries of the grains and further converted into nodal forces of the manifold elements. Under the new stress boundary condition, the NMM analysis is conducted to update the nodal positions as well as the status of intergranular contacts at the end of each time step. The updated nodal positions lead to a new geometry of soil skeleton which will be later used in the next step to update the capillary water distribution for the capillary force calculation. With cycling the above procedure through the capillary and mechanical solvers, the soil-water interaction analysis is achieved by the extended NMM with a two-way coupling procedure.

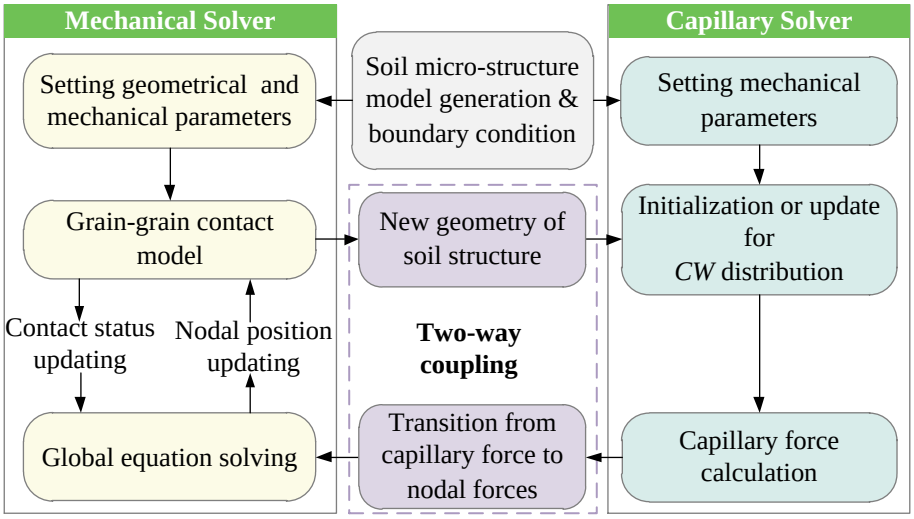

Fig. 10. Two-way coupling procedure for soil-water interaction analysis

4. Numerical Validation

This section presents two validation cases for the extended NMM scheme against analytical solutions. In Case 1, an ideal contact-disk model, which can quantitatively describe capillary water in unsaturated soil, is performed to verify the capability of the proposed capillary water solving framework in modelling the capillary water distribution and capillary force calculation. Then, the coupling approach for capillary water and soil grains is validated in Case 2, by which the relationship between shear strength and matric suction is analyzed through an ideal direct shear model. The two validation cases are respectively described below.

4.1 Case 1 - Ideal Contact-disk Model

To validate the accuracy of the capillary water solving framework in predicting the capillary water distribution and capillary force calculation, an ideal contact-disk model, which is frequently used in theoretical unsaturated soil analysis [12-17, 19], is adopted. Fig. 11(a) presents the ideal contact-disk model with four circular grains of the same radius R = 0.01 mm contacting each other at one point. The capillary water with its meniscus shape is held at the inter-grain contacts as liquid bridges. All of the capillary meniscuses (water-air interfaces) in this model have the same curvature radius r, and each of them has two ends that are tangent to the surfaces of the two grains in contact,

which implies a zero contact angle, i.e. perfect wetting [1]. According to the theoretical work by [49], the shape of the liquid bridges is defined by the curvature radius r and radius of the circular grain R, which follow the geometric relationship below:

$$r = R(\sec\alpha - 1) \tag{11}$$

where α is the half-filling angle. The total area of the capillary water A_{cw} can be expressed in terms of the half-filling angle α and the radius of the grain R:

$$A_{cw} = 8R^2\left[\tan\alpha - \alpha - (\sec\alpha - 1)^2\left(\frac{\pi}{2} - \alpha\right)\right] \tag{12}$$

When the half-filling angle α is smaller than α_c = 45°, the critical angle when the capillary meniscuses meet [1], the degree of saturation S_r of the circular grain assembly can be calculated as follows:

$$S_r = \frac{2}{4-\pi}\left[\tan\alpha - \alpha - (\sec\alpha - 1)^2\left(\frac{\pi}{2} - \alpha\right)\right] \times 100\% \tag{13}$$

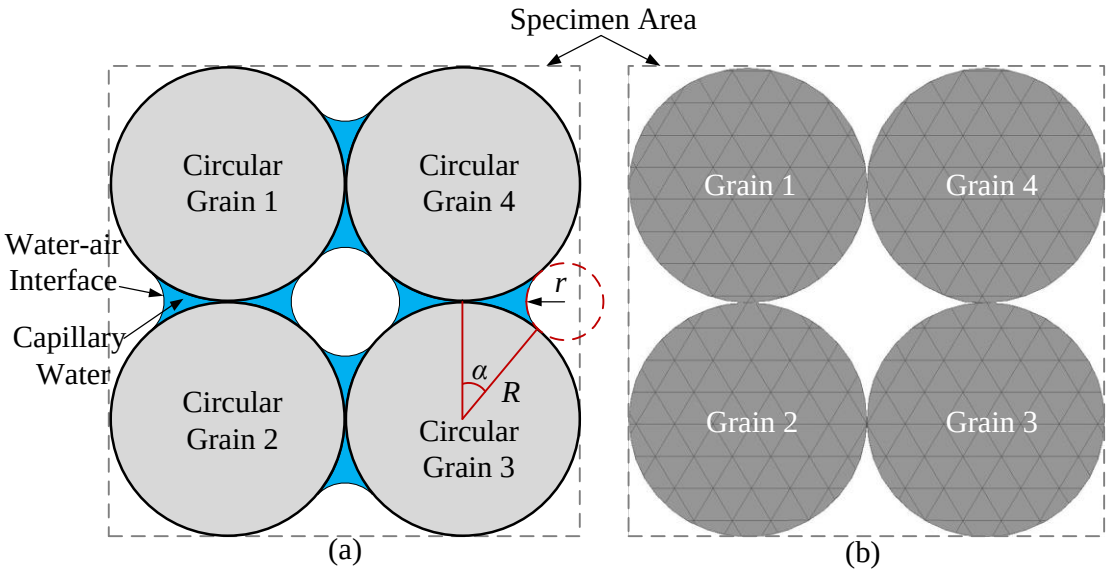

Fig. 11. Modelling capillary water distribution (a) geometry of ideal contact-disk model (b) the numerical model

To model the case by the extended NMM, a numerical model containing 319 physical patches, 4 grains and 364 manifold elements as shown in Fig. 11(b) is generated, in which the 4 grains are regular polygons with 36 sides and their positions

are fixed. To meet perfect wetting hypothesis mentioned above, the contact angles between the circular grains and water are taken as 0°. The surface tension of capillary water is set to 72.75 mN/m which is the value at a temperature of 20 ℃.

Fig. 12 shows the simulated results under different water content corresponding to different curvature radius r. The numerically predicted water contents with different curvature radius r are compared with the analytical result obtained by Eqs. (11) and (12) as shown in Fig. 13. As illustrated in the figure, the numerical result is in good agreement with the analytical solution. To further illustrate the accuracy of the proposed capillary water solving framework, the numerical soil-water characteristic curve (SWCC) of the circular grain assembly is also compared with that of the analytical solution (when $\alpha < \alpha_c$, given by Eqs. (10), (11) and (13)) as shown in Fig. 14. The above comparisons demonstrate that the capillary water distribution and its corresponding capillary forces can be successfully predicted by the proposed capillary water solving framework.

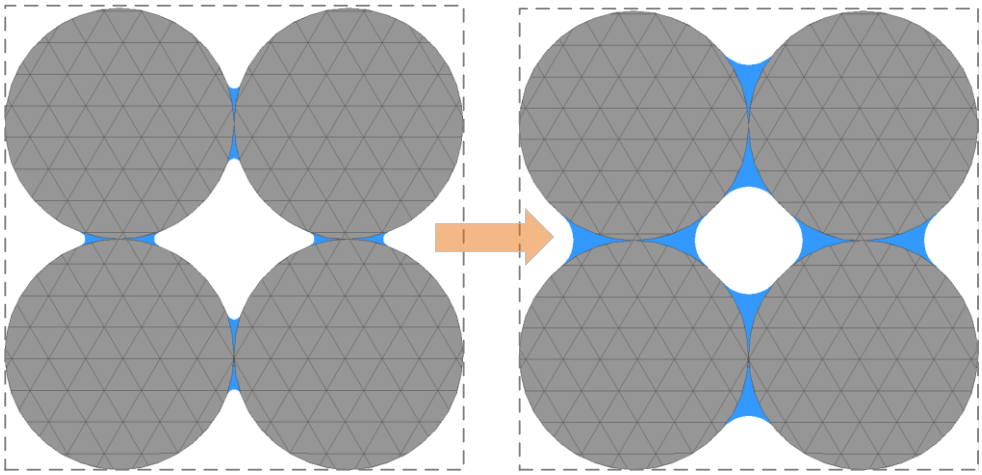

Fig. 12. Simulation results of the circular grain assembly with water content increasing

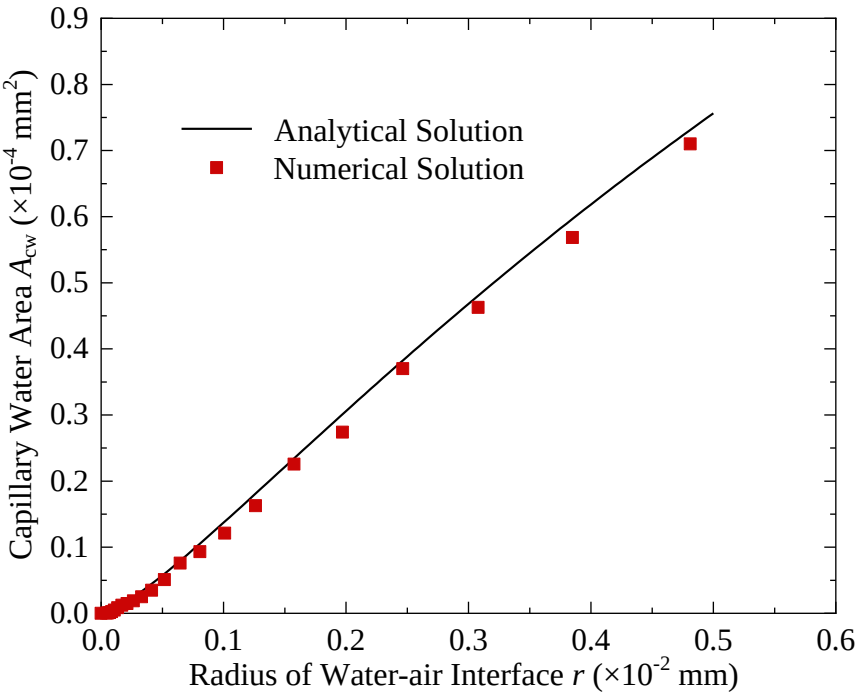

Fig. 13. Comparison between analytical and numerical capillary water area at different radius of water-air interface

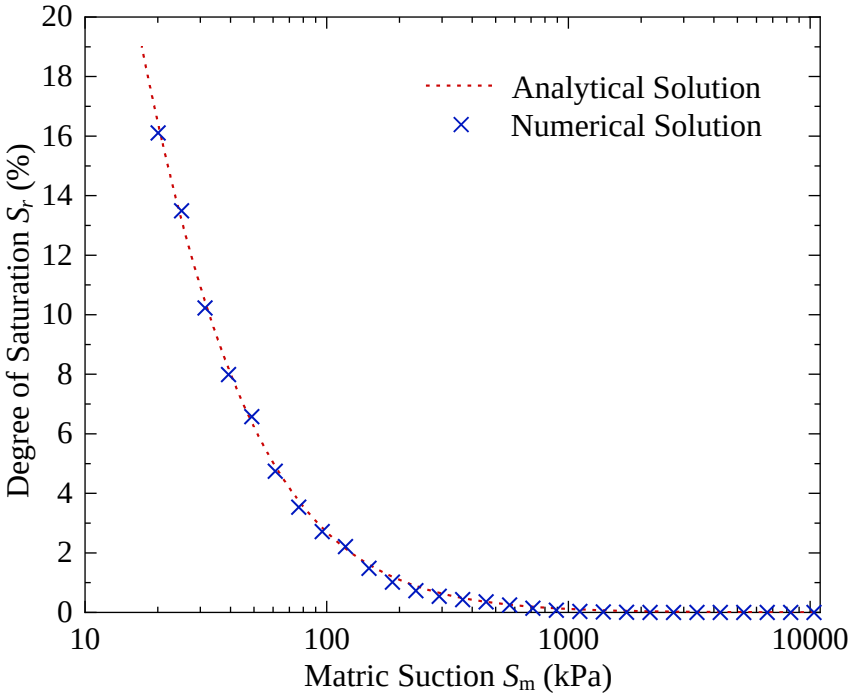

Fig. 14. Comparison between numerical and analytical solutions for the soil-water characteristic curve (SWCC)

4.2 Case 2 - Ideal Direct Shear Model

In this case, the ideal direct shear model, which developed from the ideal contact-disk model, is numerically investigated to verify the proposed two-way coupling procedure between capillary water and soil grains. As shown in Fig. 15(a), the ideal direct shear model is composed of an ideal contact-disk model with 16 circular grains of the same radius R = 0.01 mm and a shear box with dimensions of 0.15 mm × 0.09 mm. The ideal direct shear model has been studied in detail in the references [1, 2] and its matric suction-induced shear strength can be analytically expressed as follows:

$$\tau_{cap} = \frac{F_{cap}}{A}\tan\varphi' = \frac{2nT_s}{A}\left(\frac{\sin\alpha}{(\sec\alpha - 1)} + 1\right)\tan\varphi' \tag{14}$$

Where τ_{cap} is suction induced shear strength; F_{cap} is the total capillary force exerted on the shear plane; A is the area of the shear plane; α is the half-filling angle; φ' is the effective internal friction angle of the circular grain; and n is the number of the circular grains along the shear plane, which is 4 in this case.

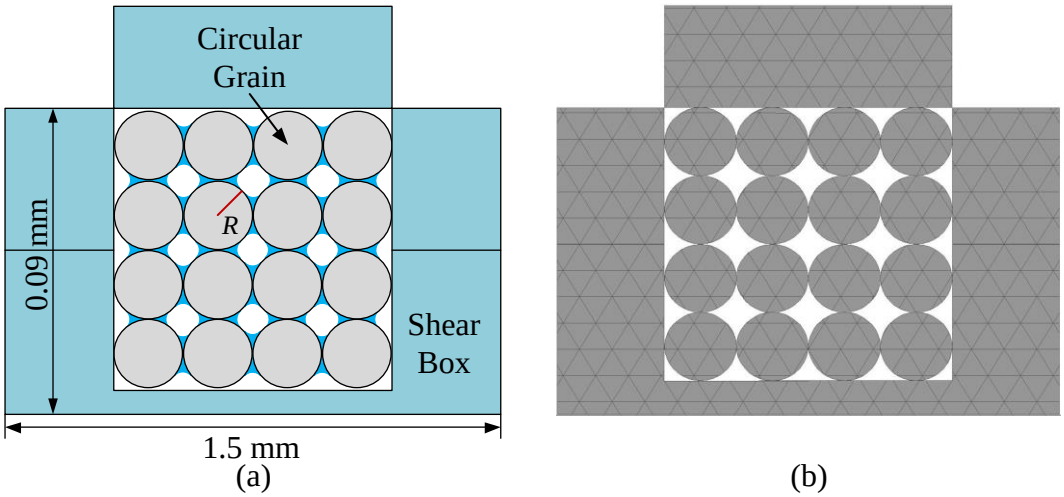

Fig. 14. Modelling ideal direct shear test (a) geometry of ideal direct shear model (b) the numerical model

As shown in Fig. 15(b), to model this case by NMM, a numerical model containing 587 physical patches and 797 manifold elements is established, in which the 16 grains are regular polygons with 36 sides. The contact angle between the circular grain and

water and surface tension of capillary water are respectively set to 0° and 72.75 mN/m at a temperature of 20 ℃. To keep the shear box free of water, the contact angle between the shear box and water is set as 180°. The other physical and mechanical parameters used in the tests are listed in Table 1. The simulated failure states of the direct shear test under different water content are presented in Fig. 16, which shows the dislocation of circular grain assembly along the shear plane and the rotation of circular grains. The numerically predicted shear strength due to matric suction is compared with the analytical solution obtained by Eq. (14) in Fig. 17. As illustrated in the figure, the numerical results generally agree well with the analytical solutions, which indicates that the proposed coupling procedure can well capture the interactions between capillary water and solid grains.

Table 1. Physical and mechanical parameters for the numerical shear test

Parameter	**Grain**	**Shear Box**
Unit mass, ρ (g/cm^3)	3.0	9.0
Young's modulus, E (GPa)	200.0	200.0
Poisson's ratio, v	0.30	0.30
Friction angle, φ (°)	25.0	0.0
Cohesion, c (MPa)	0.0	0.0
Contact angle, θ (°)	0.0	180.0

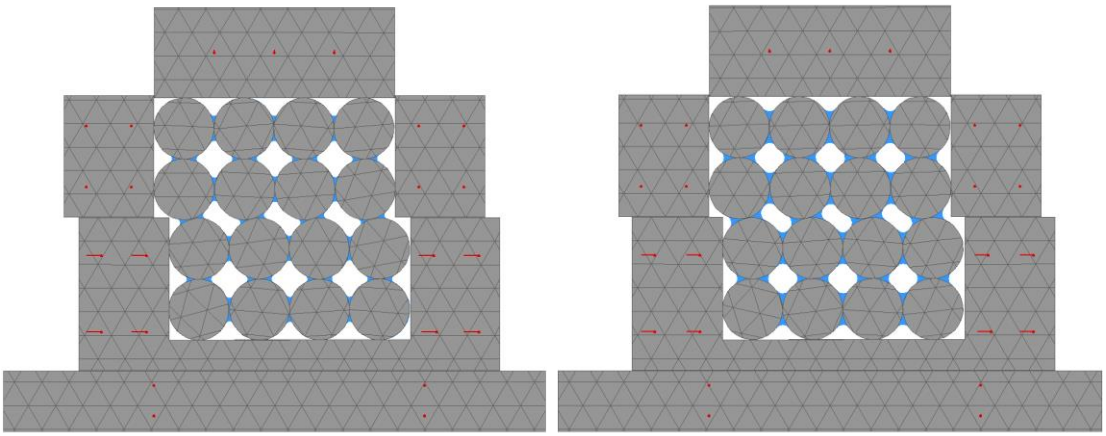

(a) (b)

Fig. 16. Simulated failure states of the direct shear test under different water content

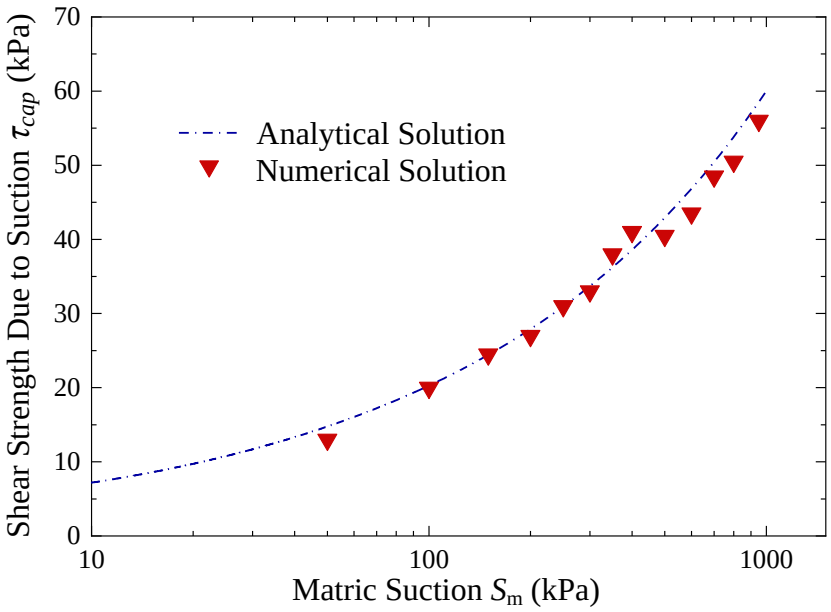

Fig. 17. Comparison between numerical and analytical solutions for the shear strength due to matric suction

5. Microscopic Simulation on Hydraulic and Mechanical characteristics of Unsaturated Soils

To study the hydraulic and mechanical characteristics of unsaturated soil at micro-scale, two soil skeleton specimens named A and B respectively are firstly established as shown in Fig. 18. These two models both have the dimensions of 0.55 mm × 0.6 mm and consists of same granular materials with same porosity P as 21% and mean grain diameter d_{50} as 0.053 mm, but different uniformity coefficients. For model A, the d_{60}/d_{10} is set to 2.7 while it is set to 1.3 for model B. The detailed grain size distributions for models A and B are shown in Fig. 19. The total numbers of soil grains in specimens A and B are 315 and 190, respectively. The Young's modulus E and Poisson's ratio v of the soil grains are set to 10 GPa and 0.3, respectively, which refers to the mechanical parameters of the granite. And the contact angles between soil grains and water are taken as 4.0° according to that between quartz and water. The two specimens are also placed in the same soil sample box with dimensions of 0.9 mm × 0.8 mm. The Young's modulus of sample box is set to 20 times that of the soil grains for controlling its deformation and the contact angle between sample box and water is taken as 60.0° with

reference to that between metal and water. The surface tension of capillary water is set as 72.75 mN/m at a temperature of 20 ℃. The other physical and mechanical parameters used in the models are listed in Table 2.

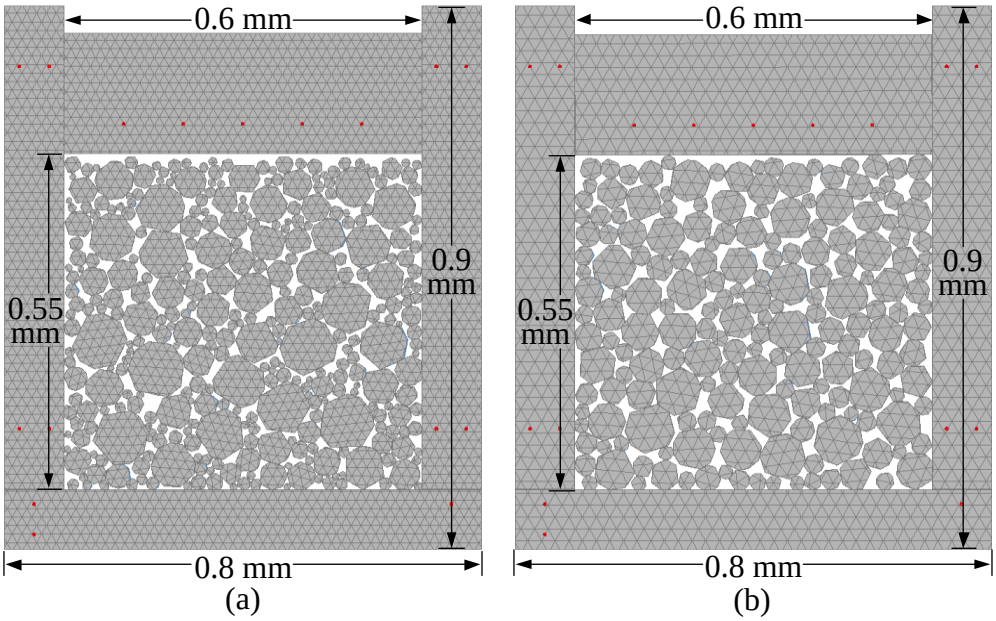

Fig. 18. The numerical models for specimens with different soil skeleton (a) A and (b) B

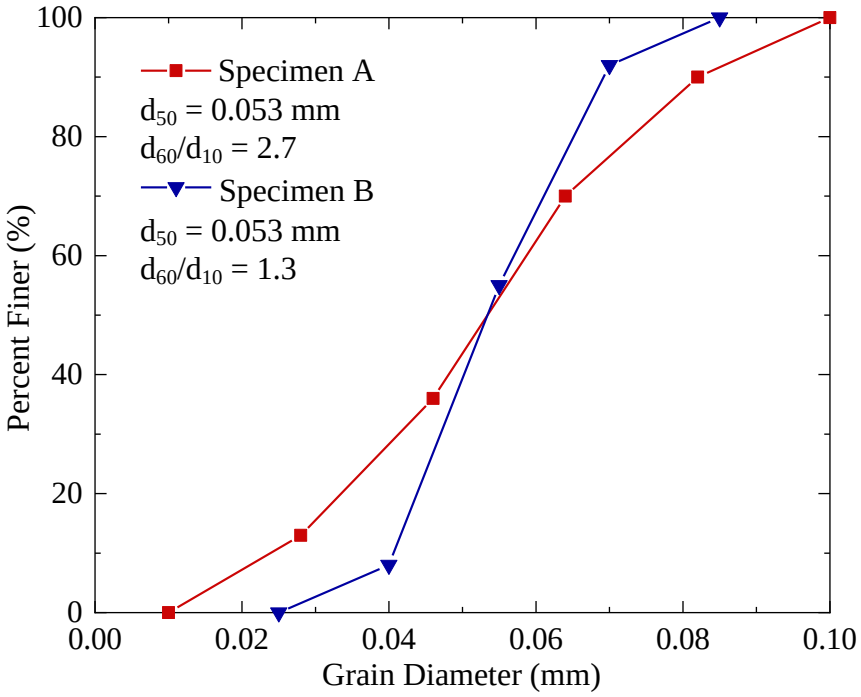

Fig. 19. Grain size distribution curves of the specimens A and B

Table 2. Physical and mechanical parameters for the specimens A and B

Parameter	**Grain**	**Sample Box**
Unit mass, ρ (g/cm^3)	2.65	9.0
Young's modulus, E (GPa)	10.0	200.0
Poisson's ratio, v	0.30	0.30
Friction angle, φ (°)	25.0	0.0
Cohesion, c (MPa)	0.0	0.0
Contact angle, θ (°)	4.0	60.0

5.1 Soil-water Characteristic Curve and Its Microscopic Exploration

Soil-water characteristic curve (SWCC) is a key parameter for unsaturated soil, which describes the relationship between water content and matric suction of unsaturated soil. As shown in Fig. 20, the numerically predicted SWCCs of the specimens A and B both exhibit the same three distinct stages divided by two inflection points when the degree of saturation S_r is about 89.0% and 3.5%, respectively. At Stage 1, S_r is very high and the matric suction S_m is very small. Then, S_m increases slightly with the decrease of S_r at Stage 2. Finally, S_m increases sharply with the decrease of S_r at Stage 3. It can also be observed from Fig. 20, despite their obvious difference in uniformity coefficients, the SWCCs of the specimens A and B are generally close except the slight discrepancy at Stage 2. This is probably because the same porosity and mean grain diameter of the specimens A and B result in their similar mean pore size. Therefore, at the same degree of saturation, the specimens A and B have a similar curvature radius of capillary meniscus, which means a close matric suction.

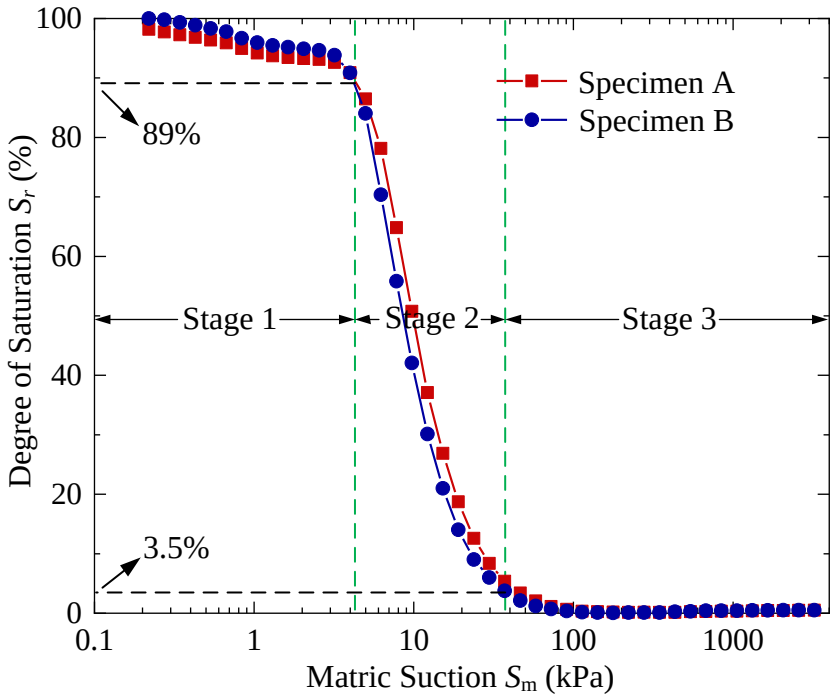

Fig. 20. Soil-water characteristic curves of the specimens A and B

In order to explore the micro-mechanism of the characteristics of the SWCCs for the specimens A and B, the evolution of the number of capillary meniscuses N and effective stress parameter χ with the degree of saturation are described in Fig. 21. χ is a key factor of Eq. (8), which represents the contribution of capillary action. In this study, χ can be calculated as:

$$\chi = \frac{\sum_n L_n^c}{\sum_n L_n^t} \tag{15}$$

where n indexing over all grains in soil specimen; L_n^c is the length of grain boundaries occupied by the capillary water; L_n^t is the total length of grain boundary. When the water content is large enough, χ can reach 1, and $\chi = 0$ for completely dry soil. Fig. 21 shows that the maximum N of specimen A is much larger than that of specimen B since specimen A has more intergranular contacts than specimen B. And the ratio of their maximum N (1.60) is close to the ratio of their numbers of soil grains (1.66). In addition, N of both specimens peaks at the same S_r of about 3.5%; and when S_r is greater than 89%, N is nearly zero. For the χ vs. S_r curves, there is a general proximity except the

small discrepancy when S_r is between 3.5% and 89% corresponding to the Stage 2 of the SWCCs of the specimens A and B. Also, when S_r is less than 3.5%, they have a steeper gradient than that when S_r is greater than 3.5%. And when S_r is greater than 89%, χ increases very slightly to approach 1.0.

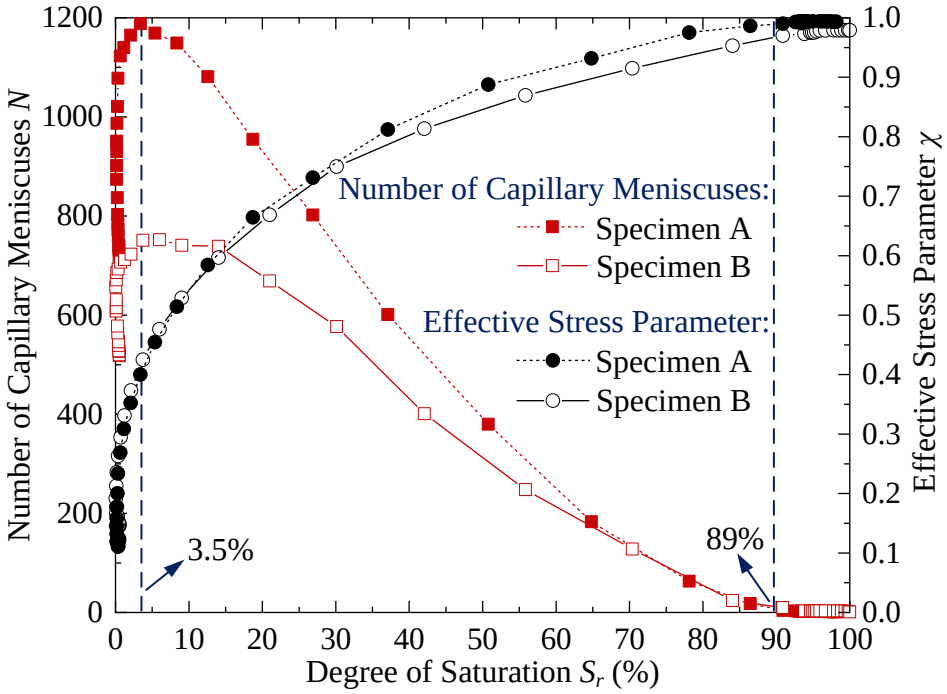

Fig. 21. Evolution of the number of capillary meniscuses N and effective stress parameter χ with the degree of saturation

As mentioned above, these two inflection points (S_r = 3.5% and S_r = 89%) reveal a close correlation among S_m, N and χ for each soil specimen. To better explain the relationship from a microscopic perspective, the specimens A and B with water content increasing are presented in Figs. 22 and 23, respectively. When the water content is very low as shown in Figs. 22(a) and 23(a), capillary water is sparsely distributed at the intergranular contacts and merely occupies a small part of the intergranular pores. At this stage, the curvature radius of capillary meniscus is very small which leads to a very large S_m. Since each liquid bridge is independent without the fusion of capillary meniscuses, N is very large. As the water content increases as shown in Figs. 22(b) and 23(b), the capillary water distributed at the intergranular contacts occupies most of the

intergranular pores. For a small number of liquid bridges, the fusion of capillary meniscuses occurs to form a locally continuous water network, which leads to the reduction of N. Meanwhile, S_m decreases due to the increase of the curvature radius of capillary meniscus. Then with further increase of the water content as shown in Figs. 22(c) and 23(c), the capillary water fills all the intergranular pores and occupies part of the trellis pores. Moreover, a large number of capillary meniscuses of liquid bridges fuse to form a globally continuous water network, resulting in a small N. Meanwhile, S_m is small due to a large curvature radius of capillary meniscus. Finally, as shown in Figs. 22(d) and 23(d), the capillary water fills almost all the pores including the intergranular and trellis pores, and there are only a few bubbles enclosed by the capillary water. N is nearly zero, since capillary meniscuses fuse at almost all liquid bridges. Moreover, the curvature radius of capillary meniscus is very large which results in a matric suction close to zero. Besides, from the above processes of increasing water content, it can be obtained that when the water content is very low, the increase of water content has a significant contribution to the increase of χ, however, when the water content is relatively large, its contribution to the increase of χ becomes smaller due to the fusion of capillary meniscuses and soil pore filling.

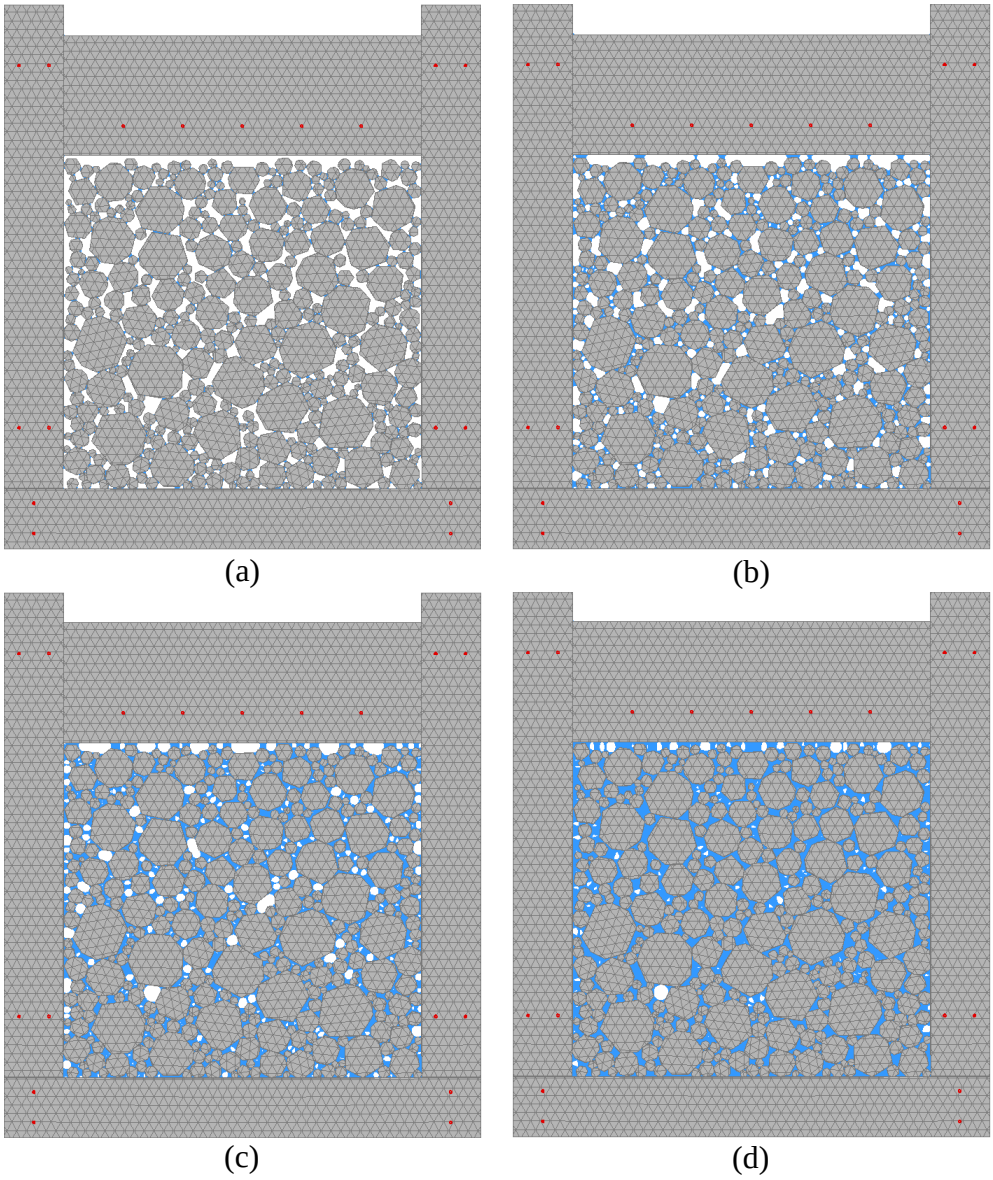

Fig. 22. The numerical model of the specimen A at different degree of saturation S_r

(a) S_r = 3.5% (b) S_r = 35% (c) S_r = 65% (d) S_r = 95%

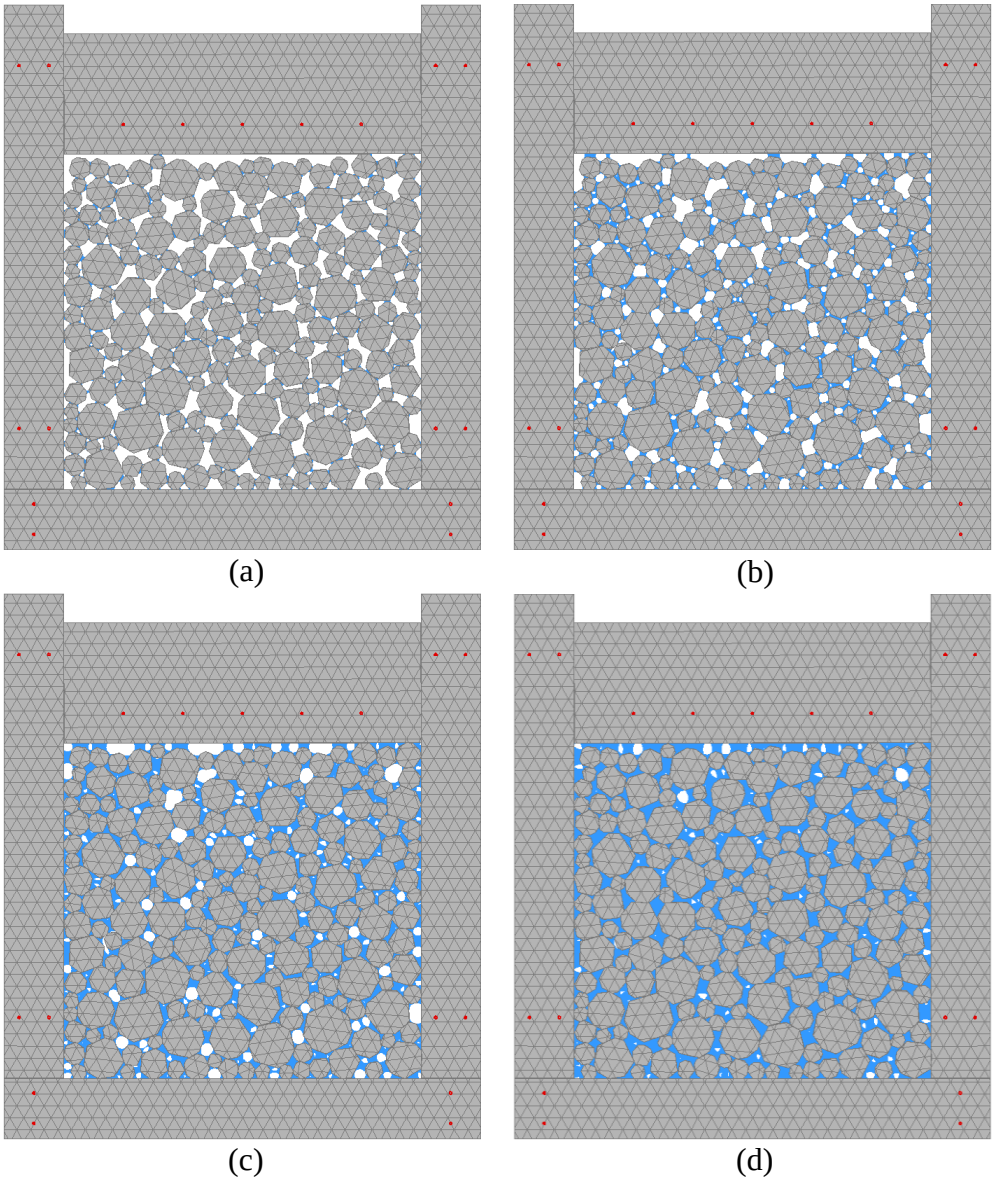

Fig. 23. The numerical model of the specimen B at different degree of saturation S_r (a) S_r = 3.5% (b) S_r = 35% (c) S_r = 65% (d) S_r = 95%

5.2 Compressibility of Unsaturated Soil and Suction Stress Characteristic Curve

To further study the effect of capillary water on mechanical behavior of unsaturated soil, numerical compression tests were respectively carried out on the dry specimens A and B as shown in Fig. 18 and wet specimens A and B with S_r = 45% as shown in Fig. 24. Each specimen is under a given uniform vertical pressure of 300 kPa exerted upon the loading plate at the top. The results of numerical compression tests on dry and wet specimens A and B are shown in Figs. 25 and 26, respectively. As shown in Figs. 25(a)

and (b), the compression displacement of wet specimen A is 0.0428 mm, which is 30.3% (0.0186 mm) less than that of dry specimen A (0.0614 mm). Similarly, as shown in Figs. 26(a) and (b), the compression displacement of wet specimen B is 0.0315 mm, which is 32.3% (0.0150 mm) less than that of dry specimen B (0.0465 mm). From the above comparisons, it can be concluded that capillary water can enhance the stiffness of unsaturated soil against compression. This is probably because there is no cohesion between soil grains, dry specimens A and B merely rely on the friction between soil grains to resist the deformation of soil skeleton against the vertical pressure. However, in addition to friction, wet specimens A and B also have the capillary forces between soil grains to contribute to the stability of soil skeleton.

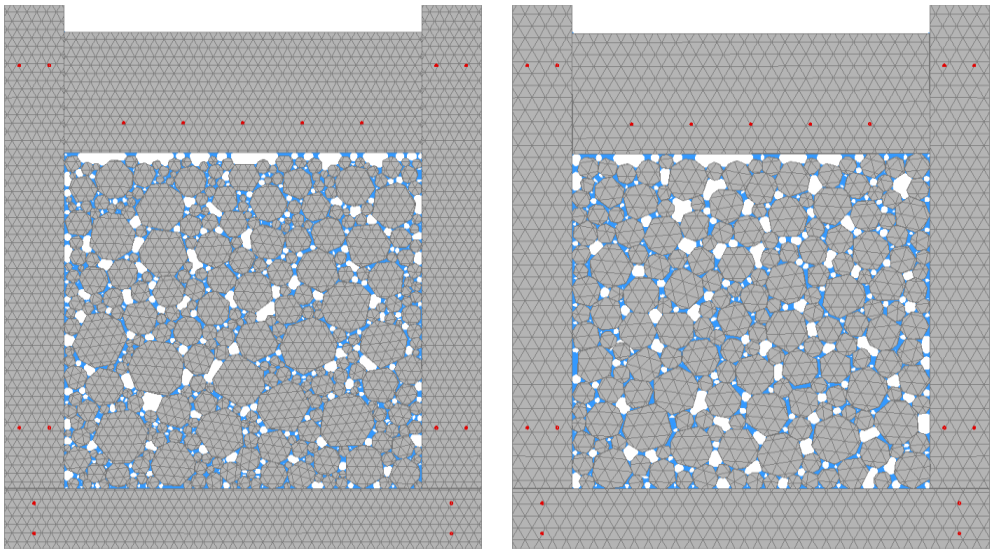

(a) (b)

Fig. 24. The numerical models of the wet specimens (a) A and (b) B at degree of saturation S_r = 45%

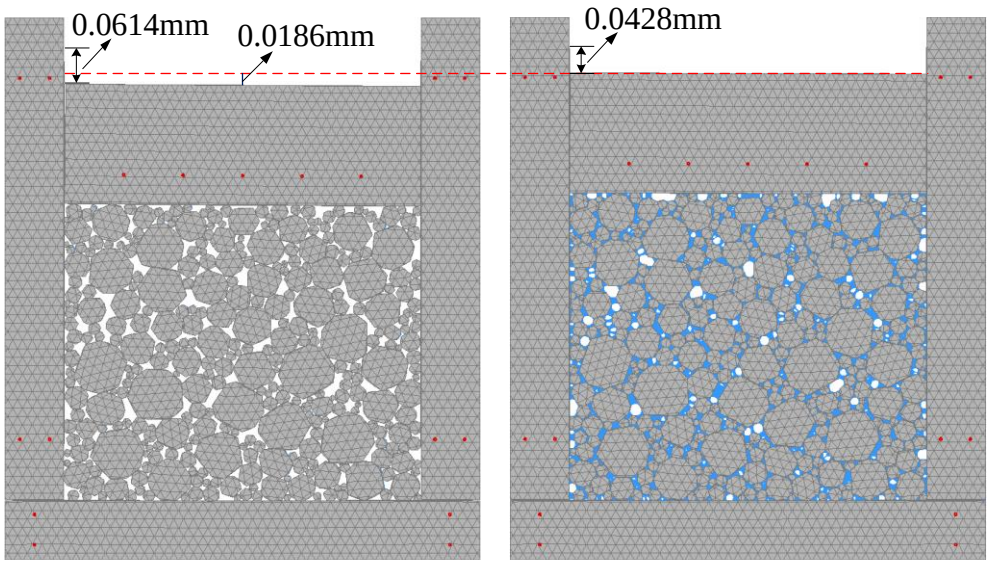

Fig. 25. Simulation results of compression tests on the (a) dry and (b) wet specimen A

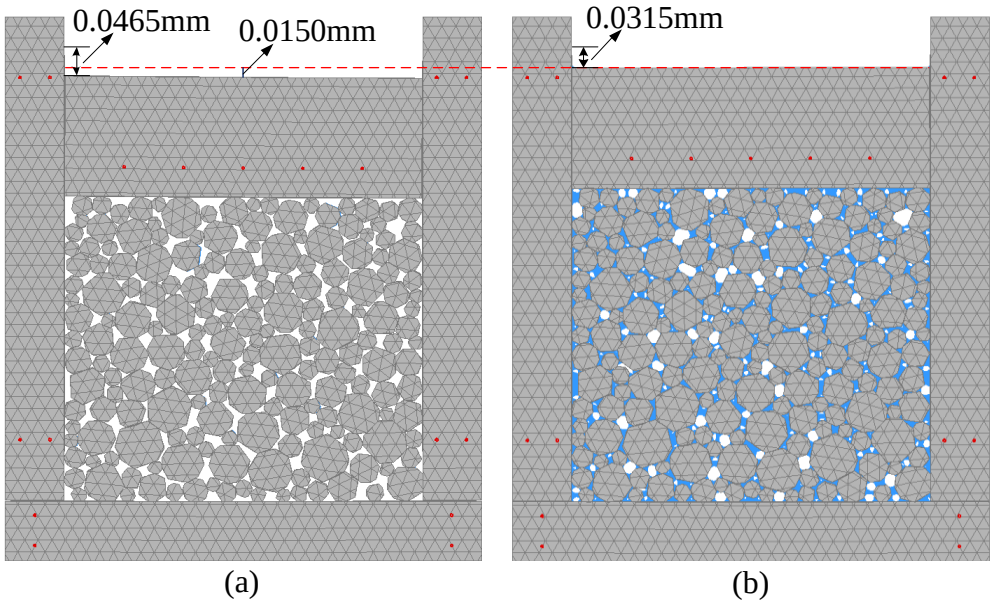

Fig. 26. Simulation results of compression tests on the (a) dry and (b) wet specimen B

After the compression tests, the soil skeleton structures become more compact with the collapse of soil pores and rotation of soil grains, which significantly affects the distribution of capillary water. In order to investigate the effect of soil skeleton structures change on hydraulic characteristics, the numerically predicted SWCCs of the wet specimens A and B before and after compression are first given in Fig. 27. As illustrated in the figure, the SWCCs of the wet specimens A and B after compression

are generally higher than that before compression in the range of about 10^{-1} kPa to 10^{2} kPa. It means that S_r after compression is larger than that before compression at the same S_m. This is because the void ratio of the wet specimens A and B decreases after compression. Therefore, at the same matric suction (i.e. the same curvature radius of capillary meniscus), capillary water can occupy a larger proportion of soil pores. However, when S_m is larger than 10^{2} kPa, since the water content of both the specimens before and after compression is very low, there is almost no difference in their saturation before and after compression at the same matric suction.

The χ vs. S_m curves and suction stress characteristic curves of the wet specimens A and B before and after compression are also simulated as shown in Figs. 28(a) and (b), respectively. When S_m is less than about 5 kPa, χ of the wet specimens A and B before and after compression are all nearly 1.0, indicating all capillary meniscuses are fused. When S_m is larger than about 5 kPa, χ of the wet specimens A and B after compression are generally larger than that before compression. The reason may be that after compression, the pore size distributions of the wet specimens A and B narrow down and thus their pore sizes become more uniform and smaller. Meanwhile, the number of intergranular contacts increases; and many angle-angle and angle-edge contacts are transformed into edge-edge contacts. Therefore, at the same matric suction (i.e. the same curvature radius of capillary meniscus), the capillary water can cover more grain boundaries after compression than that before compression, which makes χ larger. According to Eq. (8), suction stress σ^s, which represents the contribution of matric suction to the effective normal stress, is an important component of the effective normal stress and defined as the product of matric suction S_m and χ. Therefore, similar to χ, suction stress σ^s of the wet specimens A and B after compression are also generally larger than that before compression when S_m is larger than about 5 kPa, as shown in Figs. 28(a) and (b), respectively. From the above investigations, it can be suggested that the compaction of soil skeleton structure has significant effects on the hydraulic characteristics of unsaturated soil. The compacted unsaturated soil has larger degree of saturation, effective stress parameter and suction stress than before compression at the same matric suction.

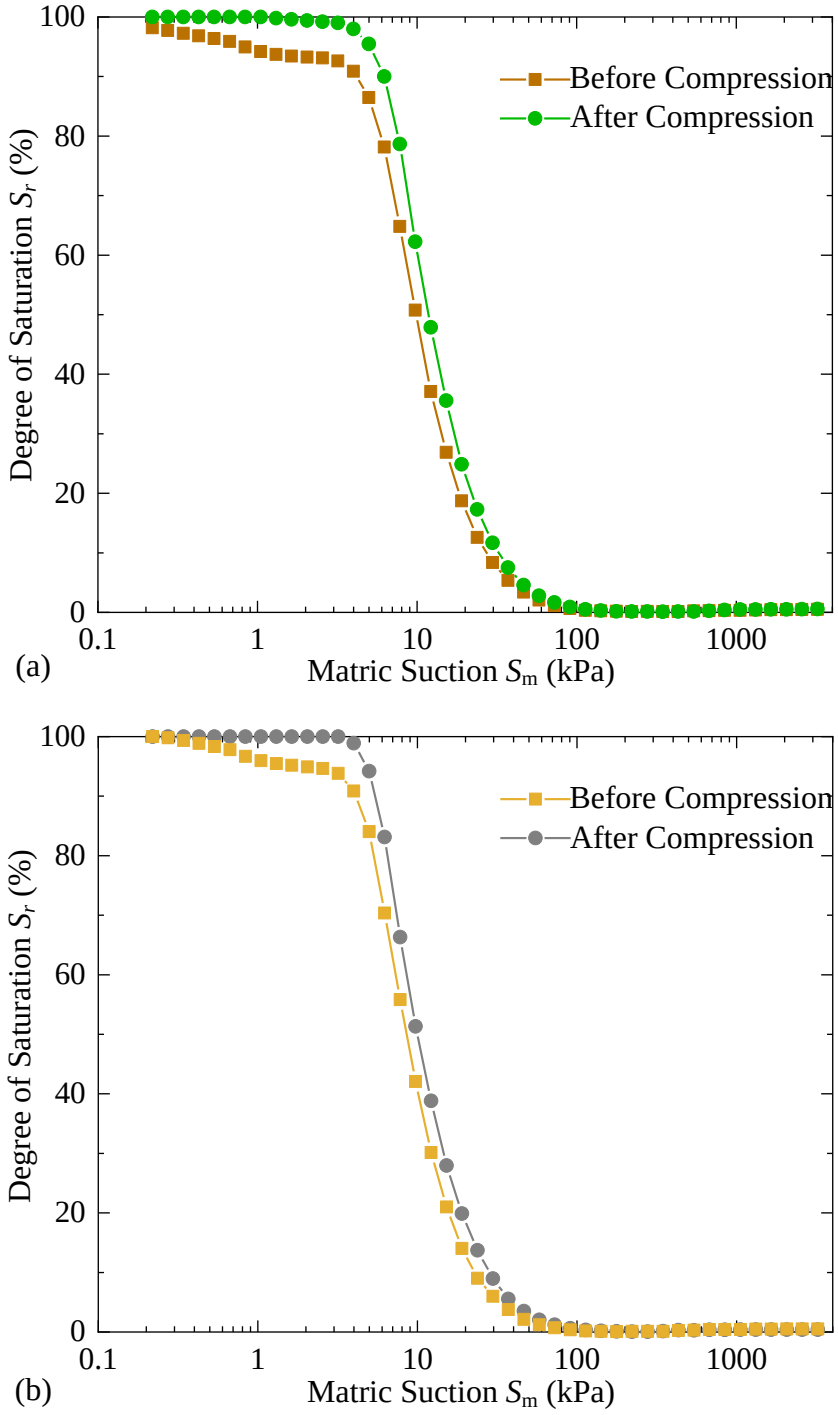

Fig. 27. Soil-water characteristic curves of the wet specimens (a) A and (b) B before and after compression

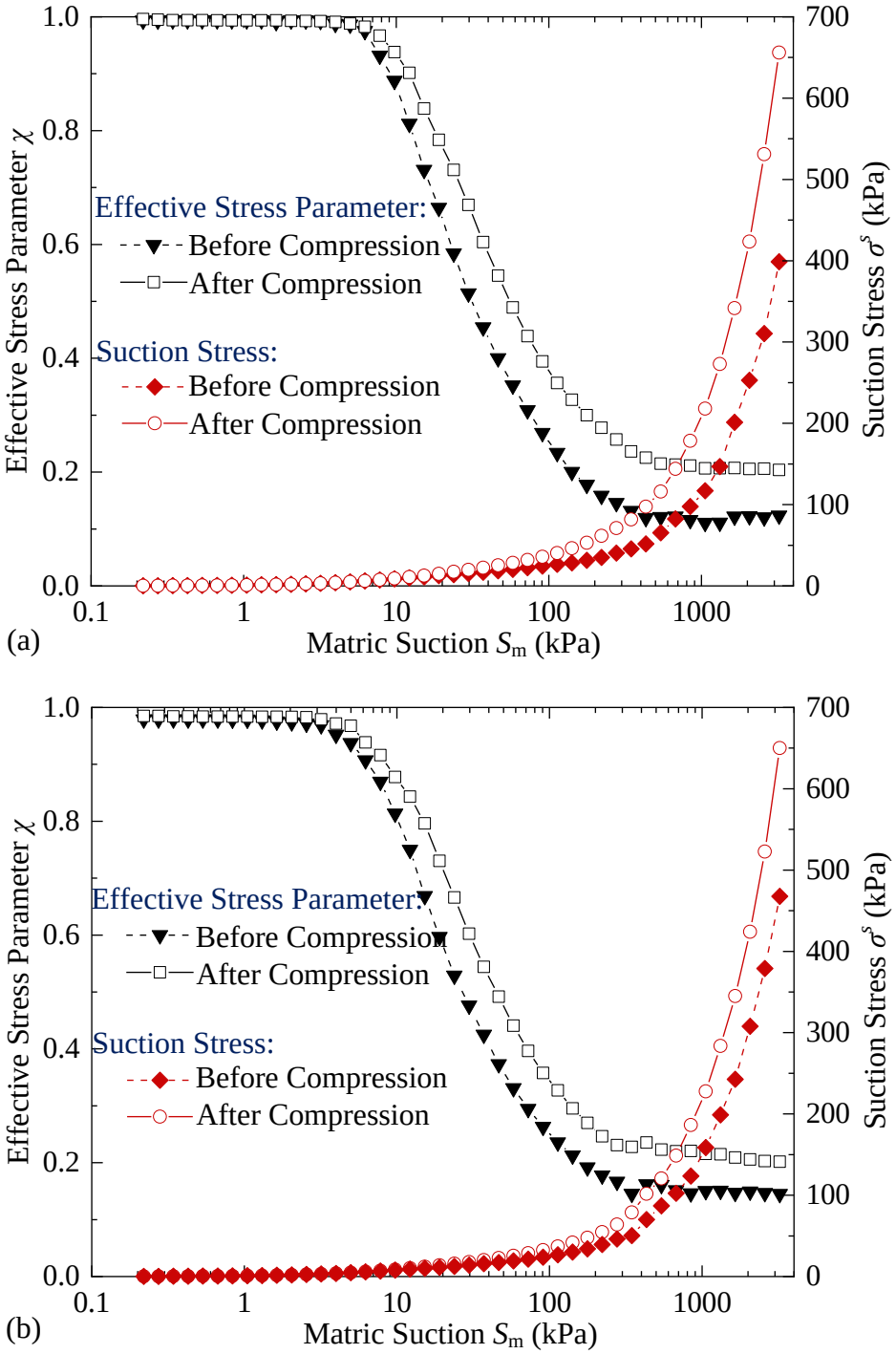

Fig. 28. Evolution of effective stress parameter χ and suction stress characteristic curves of the wet specimens (a) A and (b) B before and after compression

6. Conclusions

In this study, an extension scheme for soil-water coupling based on the NMM was proposed to analyze unsaturated soil-water interaction at micro-scale. To more

realistically model the capillary water distribution and its corresponding capillary forces of the unsaturated soil system, a capillary mechanics-based geometric algorithm is proposed. By performing the mechanical solver (NMM) and the capillary solver alternately in each time step, a two-way coupling procedure was implemented to capture the unsaturated soil-water interaction. The extended NMM was validated against analytical solutions for two ideal modeling scenarios. Further, the hydraulic and mechanical characteristics of unsaturated soil were investigated microscopically by conducting hydraulic and compression simulations on the two soil skeleton specimens of same porosity and mean grain diameter but different uniformity coefficients. The main conclusions drawn from the study are as follows:

- Based on the capillary mechanics-based geometric algorithm and the Young-Laplace equation, the capillary solver can satisfactorily predict the capillary water distribution and its corresponding capillary forces as well as the SWCC of the unsaturated soil system.
- By performing the mechanical solver (NMM) and the capillary solver alternately in each time step, the extended NMM with a two-way coupling procedure can capture sufficiently the mechanical behaviour of unsaturated soil under compression and shear.
- For soil specimens of same porosity and mean grain diameter, despite the difference of uniformity coefficients, their SWCCs are similar. In addition, for each soil specimen, there is a close correlation among S_m, N and χ. With the increase of water content, the curvature radius of capillary meniscus increases, resulting in the decrease of S_m. Meanwhile, more and more capillary meniscuses fuse to reduce N to approach zero. Also, the increase of χ with water content slows down due to both the fusion of capillary meniscuses and soil pore filling.
- Due to the capillary forces between soil grains, capillary water can enhance the stiffness of unsaturated soil against compression. Furthermore, the compaction of soil skeleton structure has significant effects on the hydraulic characteristics of unsaturated soil. The compacted unsaturated soil has larger

degree of saturation, effective stress parameter and suction stress than before compression at the same matric suction.

Acknowledgements

The research work is supported by the National Natural Science Foundation of China (Grant nos. 41502283, 41772309) and the China Scholarship Council (Grant no. 201906270145).

References

[1] M.J. Jiang, S. Leroueil, J.M. Konrad, Insight into shear strength functions of unsaturated granulates by DEM analyses, Computers and Geotechnics, 31 (2004) 473-489.
[2] Z. Shen, M. Jiang, C. Thornton, Shear strength of unsaturated granular soils: three-dimensional discrete element analyses, Granular Matter, 18 (2016).
[3] L.J. Briggs, mechanics of soil moisture, (1897).
[4] W.B. Haines, Studies in the physical properties of soils: IV. A further contribution to the theory of capillary phenomena in soil, The Journal of Agricultural Science, 17 (1927) 264-290.
[5] K. Terazaghi, Theoretical soil mechanics, John Wiley Sons, (1965).
[6] A.W. Bishop, The principle of effective stress, Teknisk Ukeblad, 39 (1959) 859-863.
[7] A.W. Bishop, G. Blight, Some aspects of effective stress in saturated and partly saturated soils, Geotechnique, 13 (1963) 177-197.
[8] D. Fredlund, N.R. Morgenstern, R. Widger, The shear strength of unsaturated soils, Canadian Geotechnical Journal, 15 (1978) 313-321.
[9] W.S. Kim, R.H. Borden, Influence of soil type and stress state on predicting shear strength of unsaturated soils using the soil-water characteristic curve, Canadian Geotechnical Journal, 48 (2011) 1886-1900.
[10] D. Sheng, A. Zhou, D.G. Fredlund, Shear strength criteria for unsaturated soils, Geotechnical and Geological Engineering, 29 (2011) 145-159.
[11] S. Vanapalli, D. Fredlund, D. Pufahl, A. Clifton, Model for the prediction of shear strength with respect to soil suction, Canadian Geotechnical Journal, 33 (1996) 379-392.
[12] R. Fisher, On the capillary forces in an ideal soil; correction of formulae given by WB Haines, The Journal of Agricultural Science, 16 (1926) 492-505.
[13] A. Sparks, Theoretical considerations of stress equations for partly saturated soils, Civil Eng Bull, Capetown Univ/S Afr/, (1965).
[14] G.C. Cho, J.C. Santamarina, Unsaturated Particulate Materials—Particle-Level Studies, Journal of Geotechnical and Geoenvironmental Engineering, 127 (2001) 84-96.
[15] G. Lian, C. Thornton, M.J. Adams, A Theoretical Study of the Liquid Bridge

Forces between Two Rigid Spherical Bodies, Journal of Colloid Interface Science, 161 (1993) 138-147.
[16] G. Mason, W. Clark, Liquid bridges between spheres, Chemical Engineering Science, 20 (1965) 859-866.
[17] W.J. Likos, N. Lu, Hysteresis of capillary stress in unsaturated granular soil, Journal of Engineering mechanics, 130 (2004) 646-655.
[18] R. Wan, S. Khosravani, F. Nicot, Micromechanical analysis of stress in an unsatured granular medium, in: The 2nd International Symposium on Computational Geomechanics (ComGeo II), Cavtat-Dubrovnik, 2011.
[19] J. Lechman, N. Lu, Capillary Force and Water Retention between Two Uneven-Sized Particles, Journal of Engineering Mechanics, 134 (2008) 374-384.
[20] X. Li, Effective stress in unsaturated soil: a microstructural analysis, Géotechnique, 53 (2003) 273-277.
[21] X. Lee, W.C. Dass, C.W. Manzione, Characterization of granular material composite structures using computerized tomography, in: Engineering Mechanics, ASCE, 1992, pp. 268-271.
[22] T.S. Majmudar, R.P. Behringer, Contact force measurements and stress-induced anisotropy in granular materials, Nature, 435 (2005) 1079-1082.
[23] H. Zheng, T. Zhang, Q. Wang, The mixed complementarity problem arising from non-associative plasticity with non-smooth yield surfaces, Computer Methods in Applied Mechanics and Engineering, 361 (2020).
[24] F. Xiong, Q. Jiang, C. Xu, X. Zhang, Q. Zhang, Influences of connectivity and conductivity on nonlinear flow behaviours through three-dimension discrete fracture networks, Computers and Geotechnics, 107 (2019) 128-141.
[25] F. Xiong, W. Wei, C. Xu, Q. Jiang, Experimental and numerical investigation on nonlinear flow behaviour through three dimensional fracture intersections and fracture networks, Computers and Geotechnics, 121 (2020).
[26] D. Liu, L. Hou, C. Wu, Numerical analysis for unsaturated soil slope which locates on reservoir region and under the condition of water level fluctuation, Journal of Information and Computational Science, 9 (2012) 2719-2729.
[27] Z. Zheng, L. Hou, C. Wu, Stability of slope which locates on reservoir region and the corresponding influence mechanisms induced by fluctuation of water level, in: 2011 International Conference on Multimedia Technology, IEEE, 2011, pp. 4591-4595.
[28] W. Ehlers, T. Graf, M. Ammann, Deformation and localization analysis of partially saturated soil, Computer Methods in Applied Mechanics and Engineering, 193 (2004) 2885-2910.
[29] J. Ghorbani, D.W. Airey, A. El-Zein, Numerical framework for considering the dependency of SWCCs on volume changes and their hysteretic responses in modelling elasto-plastic response of unsaturated soils, Computer Methods in Applied Mechanics and Engineering, 336 (2018) 80-110.
[30] K. Wang, X. Song, Strain localization in non-isothermal unsaturated porous media considering material heterogeneity with stabilized mixed finite elements, Computer Methods in Applied Mechanics and Engineering, 359 (2020).
[31] W. Wu, Y. Yang, H. Zheng, Hydro-mechanical simulation of the saturated and

semi-saturated porous soil–rock mixtures using the numerical manifold method, Computer Methods in Applied Mechanics and Engineering, 370 (2020).
[32] P.A. Cundall, O.D. Strack, A discrete numerical model for granular assemblies, Geotechnique, 29 (1979) 47-65.
[33] A. Anandarajah, On influence of fabric anisotropy on the stress-strain behavior of clays, Computers and Geotechnics, 27 (2000) 1-17.
[34] M. Jiang, Z. Shen, C. Thornton, Microscopic contact model of lunar regolith for high efficiency discrete element analyses, Computers and Geotechnics, 54 (2013) 104-116.
[35] M. Jiang, H.-S. Yu, S. Leroueil, A simple and efficient approach to capturing bonding effect in naturally microstructured sands by discrete element method, International Journal for Numerical Methods in Engineering, 69 (2007) 1158-1193.
[36] M.J. Jiang, J.M. Konrad, S. Leroueil, An efficient technique for generating homogeneous specimens for DEM studies, Computers and Geotechnics, 30 (2003) 579-597.
[37] Z. Shen, M. Jiang, C. Thornton, DEM simulation of bonded granular material. Part I: Contact model and application to cemented sand, Computers and Geotechnics, 75 (2016) 192-209.
[38] C. Thornton, Numerical simulations of deviatoric shear deformation of granular media, Géotechnique, 50 (2000) 43-53.
[39] J.M. Ting, B.T. Corkum, C.R. Kauffman, C. Greco, Discrete numerical model for soil mechanics, Journal of Geotechnical Engineering, 115 (1989) 379-398.
[40] U. El Shamy, T. Gröger, Micromechanical aspects of the shear strength of wet granular soils, International Journal for Numerical and Analytical Methods in Geomechanics, 32 (2008) 1763-1790.
[41] J.A. Gili, E.E. Alonso, Microstructural deformation mechanisms of unsaturated granular soils, International Journal for Numerical and Analytical Methods in Geomechanics, 26 (2002) 433-468.
[42] S.H. Liu, D.A. Sun, Simulating the collapse of unsaturated soil by DEM, International Journal for Numerical and Analytical Methods in Geomechanics, 26 (2002) 633-646.
[43] S.H. Liu, D.A. Sun, Y. Wang, Numerical study of soil collapse behavior by discrete element modelling, Computers and Geotechnics, 30 (2003) 399-408.
[44] V. Richefeu, M.S. El Youssoufi, R. Peyroux, F. Radjaï, A model of capillary cohesion for numerical simulations of 3D polydisperse granular media, International Journal for Numerical and Analytical Methods in Geomechanics, 32 (2008) 1365-1383.
[45] L. Scholtès, P.Y. Hicher, F. Nicot, B. Chareyre, F. Darve, On the capillary stress tensor in wet granular materials, International Journal for Numerical and Analytical Methods in Geomechanics, 33 (2009) 1289-1313.
[46] S. Ma, Z. Zhao, W. Nie, J. Nemcik, Z. Zhang, X. Zhu, Implementation of displacement-dependent Barton-Bandis rock joint model into discontinuous deformation analysis, Computers and Geotechnics, 86 (2017) 1-8.
[47] Y. Ning, Z. Yang, B. Wei, B. Gu, Advances in two-dimensional discontinuous deformation analysis for rock-mass dynamics, International Journal of Geomechanics,

17 (2017) E6016001.
[48] G.-x. Zhang, G. Li, R. Guo, Stress-strain relationship for soil using discontinuous deformation analysis, JOURNAL-TSINGHUA UNIVERSITY, 40 (2000) 102-105.
[49] L. Guo, T. Li, G. Chen, P. Yu, X. Peng, D. Yang, A method for microscopic unsaturated soil-water interaction analysis based on DDA, Computers and Geotechnics, 108 (2019) 143-151.
[50] F. Radjai, V. Richefeu, Bond anisotropy and cohesion of wet granular materials, Philos Trans A Math Phys Eng Sci, 367 (2009) 5123-5138.
[51] G. Ma, X. An, L. He, The numerical manifold method: a review, International Journal of Computational Methods, 7 (2010) 1-32.
[52] G.-H. Shi, Manifold method of material analysis, in, Army Research Office Research Triangle Park NC, 1992.
[53] M. Hu, J. Rutqvist, Y. Wang, A numerical manifold method model for analyzing fully coupled hydro-mechanical processes in porous rock masses with discrete fractures, Advances in Water Resources, 102 (2017) 111-126.
[54] G. Kang, P. Chen, X. Guo, G. Ma, Y. Ning, Simulations of meso-scale deformation and damage of polymer bonded explosives by the numerical manifold method, Engineering Analysis with Boundary Elements, 96 (2018) 123-137.
[55] X. Li, Q. Zhang, J. Li, J. Zhao, A numerical study of rock scratch tests using the particle-based numerical manifold method, Tunnelling and Underground Space Technology, 78 (2018) 106-114.
[56] G. Ma, X. An, H. Zhang, L. Li, Modeling complex crack problems using the numerical manifold method, International Journal of Fracture, 156 (2009) 21-35.
[57] Y.J. Ning, X.M. An, G.W. Ma, Footwall slope stability analysis with the numerical manifold method, International Journal of Rock Mechanics and Mining Sciences, 48 (2011) 964-975.
[58] Y. Yang, X. Tang, H. Zheng, Q. Liu, L. He, Three-dimensional fracture propagation with numerical manifold method, Engineering Analysis with Boundary Elements, 72 (2016) 65-77.
[59] H.H. Zhang, L.X. Li, X.M. An, G.W. Ma, Numerical analysis of 2-D crack propagation problems using the numerical manifold method, Engineering Analysis with Boundary Elements, 34 (2010) 41-50.
[60] G.F. Zhao, X.B. Zhao, J.B. Zhu, Application of the numerical manifold method for stress wave propagation across rock masses, International Journal for Numerical and Analytical Methods in Geomechanics, 38 (2014) 92-110.
[61] H. Zheng, D. Xu, New strategies for some issues of numerical manifold method in simulation of crack propagation, International Journal for Numerical Methods in Engineering, 97 (2014) 986-1010.
[62] Z. Wu, L. Fan, Q. Liu, G. Ma, Micro-mechanical modeling of the macro-mechanical response and fracture behavior of rock using the numerical manifold method, Engineering Geology, 225 (2017) 49-60.
[63] Z. Wu, H. Sun, L.N.Y. Wong, A Cohesive Element-Based Numerical Manifold Method for Hydraulic Fracturing Modelling with Voronoi Grains, Rock Mechanics and Rock Engineering, 52 (2019) 2335-2359.

[64] H. Zheng, F. Wang, The numerical manifold method for exterior problems, Computer Methods in Applied Mechanics and Engineering, 364 (2020).
[65] J.S. Lin, A mesh-based partition of unity method for discontinuity modeling, Computer Methods in Applied Mechanics and Engineering, 192 (2003) 1515-1532.
[66] Z. Wu, W. Cui, L. Fan, Q. Liu, Mesomechanism of the dynamic tensile fracture and fragmentation behaviour of concrete with heterogeneous mesostructure, Construction and Building Materials, 217 (2019) 573-591.
[67] Z. Wu, L.N.Y. Wong, Extension of numerical manifold method for coupled fluid flow and fracturing problems, International Journal for Numerical and Analytical Methods in Geomechanics, 38 (2014) 1990-2008.